Investigation of Uniform Plasma Channel Generation for Short Laser Pulse Amplification

Joel Greenberg

Submitted to the
Department of Mechanical and Aerospace Engineering
Princeton University
in partial fulfillment of the requirements of
Undergraduate Senior Thesis

Final Report
April 28, 2005

Advisor: Szymon Suckewer
Reader: Richard Miles
MAE 442
89 pages
Color Printing

Honor Code

On my honor, I pledge that this senior thesis represents my own work in accordance with university regulations.

Joel Greenberg   4/28/05

Dedication

For my family for their support and encouragement,

For my friends for the last four years,

And for my fiancee for everything.

Abstract

Due to the various limitations of current ultrashort pulse laser amplification techniques at very high powers, new methods must be invented in order to proceed into new regimes of laser power. One such method for amplification is the resonant Raman backscattering scheme whereby plasma is used as the coupling medium between two counterpropogating pulses. This method has been successfully demonstrated by Suckewer *et al.* [11] to produce subpicosecond pulses with amplification up to 100 times via a gas-jet plasma. Unfortunately, the amplification process is limited by both the uniformity and the length of the produced plasma. The goal of this experiment is to explore other techniques for plasma production with a focus on producing plasmas more suitable for use in the Raman backscattering amplification regime. In this experiment, a quiet gas contained within a gas cell is used as the ionizing medium and is ionized via a subnanosecond laser pulse. Scans over a number of different parameters are performed in order to determine the optimal conditions for the plasma formation as well as to further understand the processes involved in the plasma formation. Diagnostics have been developed for extraction of key plasma parameters over a range of different times. The final result is a 2.5 mm plasma with a nonuniformity ±3.5 % produced in N_2 at ~70 torr.

Acknowledgements

This research is only a subset of work being done by numerous members of both the Princeton University and Princeton Plasma Physics Lab community.

I would like to thank my advisor, Professor Szymon Suckewer, who has taught me much about plasmas and various applications of quantum mechanics as well as helped to guide and structure my independent thesis research throughout the year.

Much of this work is also thanks, in part, to Dr. Alexander Dunaevsky who has spent countless hours with me in the lab both helping me with the experiment and teaching me about many other important things. Also, I would like to thank Anatoli Morozov for his help on the experiment as well as for the time he spent educating me about the art of laser alignment.

Special thanks goes to Nick Tkach – our superb technician. Not only does he keep everything working in the lab, but you can always find whatever you need in and among his supplies.

Finally, thanks to Dr. Alexander Goltsov and Daniel Broaddus (a former Princeton student) for their work on the experimental setup prior to my arrival on the project.

Contents

List of Figures

List of Symbols

ω_{plasma}: plasma frequency

ω_{seed}: seed frequency

ω_{pump}: pump frequency

P: polarizability

e: charge of an electron

n_e: electron density

I: laser intensity

λ: laser wavelength

E: electric field strength of laser

p: pressure

d: distance between cathode and anode

k: wave number

l: length of KDP crystal

c: speed of light

w: beam waist

u_0: the spatial carrier frequency of the interference pattern

a(x, y): represents the low-frequency background intensity

b(x, y): is the local fringe visibility

$\Phi(x, y)$: is the local fringe phase

n_{cr}: critical density

N: index of refraction

ε_q: ponderomotive potential

A,B, γ: empirical constants for gas breakdown

I_p: ionization potential

L: length of pump pulse

Z_r: Rayleigh length

ρ_0: gas density

Chapter 1

Introduction

Ultrashort laser technology has been of crucial importance to many areas of research both from a scientific and technological standpoint. While many of the basic principles have been known for a relatively long time, new techniques and schemes are being developed which allow for previous technical challenges to be overcome and new phenomena and regimes to be probed. The applications of such high power and short pulse lasers are widespread and extremely interdisciplinary in nature. A more powerful ultrashort laser pulse can be used as a diagnostic instrument for ultrafast molecular spectroscopy or as a tool in micromachining. These high power lasers can also be used in a variety of other fields such as plasma physics (petawatt (10^{15}W) lasers are integral to studying fast ignition for inertial confinement fusion), accelerator physics (for use in laser wake field accelerators), as well as laser physics (where applications to high harmonic generation and the further development of soft x-ray lasers would benefit from new laser technology). Beyond purely scientific applications, high power ultrashort lasers have a variety of applications in the field of medicine through venues such as improving precision nanosurgery and bettering the treatment of various diseases. In order to continue beyond current limitations, a new form of ultrashort pulse amplification via resonant Raman backscattering (RBS) has been proposed which makes use of plasma as an amplifying medium. The goals of this work are to: 1) create a longer, more uniform plasma channel than previously achieved; and 2) better understand the processes which contribute to plasma generation as well as how it is affected by different key parameters. Beyond the proposed RBS amplification scheme, advances in the production of uniform plasma channels have applications to processes such as plasma waveguiding of ultrashort pulses as well as providing a clean geometry by which to confirm various models of plasma behavior. Thus, advances in plasma generation are important to the future of many engineering and experimental methods.

1.1 Chirped Pulse Amplification (CPA)

Prior to CPA laser systems, high power solid state lasers used an architecture which consisted of a monochromatic oscillator that produced a high quality seed pulse of several hundred picoseconds (ps=10^{-12}s) in duration, followed by an amplifier or amplifier chain that raised the seed pulse's energy to the gigawatt (GW=10^{9} W) range. Above this threshold, problems of self-focusing, filamentation, self-phase modulation, nonlinear optical damage, and saturation provided a ceiling to the achievable amplification of laser pulses. In recent years (since the 1990s), new laser technologies have succeeded in producing laser pulses on the order of 20-femtoseconds (fs=10^{-15}s) with powers in the multi-terawatt (TW=10^{12}W) range. The most frequent technique used to achieve such high-power ultrashort laser pulses is the method of chirped pulse amplification (see Fig. 1.1 a). CPA is a three step process which avoids the problems previously mentioned. The first stage of CPA uses optical gratings to expand a low-energy, short pulse into its frequency components and then reorder them into a time-stretched lower-peak-intensity pulse of the same energy (with an amplitude reduced by a factor equal to its temporal stretching). This temporal broadening is accomplished through noting that, upon striking the diffraction grating, the pulse spreads out at an angle with each frequency component leaving at a slightly different dispersed angle. Each particular frequency then travels a slightly different optical path allowing each to arrive at the next stage at staggered times, thus resulting in the temporal ordering (with the pulse being ‘redder’ at the front). In the second stage, a broadband optical amplifier is employed to amplify the energy of the frequency components individually. In the final stage, the original wave is recompressed into a highly amplified signal by compressing the pulse via complementary gratings. This final pulse can have energies well beyond those possible in previous methods while avoiding many of the intensity-related issues inherent in them. Also, due to reduced heating of the amplifier bulk optical medium, a CPA laser can be fired in shorter intervals than in previous methods [1].

While this method has been highly successful in reliably producing very high power lasers, the methodology of CPA begins to be burdensome in approaching the petawatt scale. One of the main limitations of CPA derives from the final compression grating’s inability to withstand the high intensity pulse it is reconstructing. The fluence limit of the compression gratings is generally less than 5 J/cm^2 for subpicosecond pulses [2], thus physically disallowing amplification. Also, from a logistical standpoint, there are numerous technical and economical challenges in producing the increasingly large, high quality optics needed in CPA. In order to reach the petawatt scale, gratings approximately a meter in diameter are required and, because the efficiency of the amplification is affected by the exactness of recompression at the final grating, the

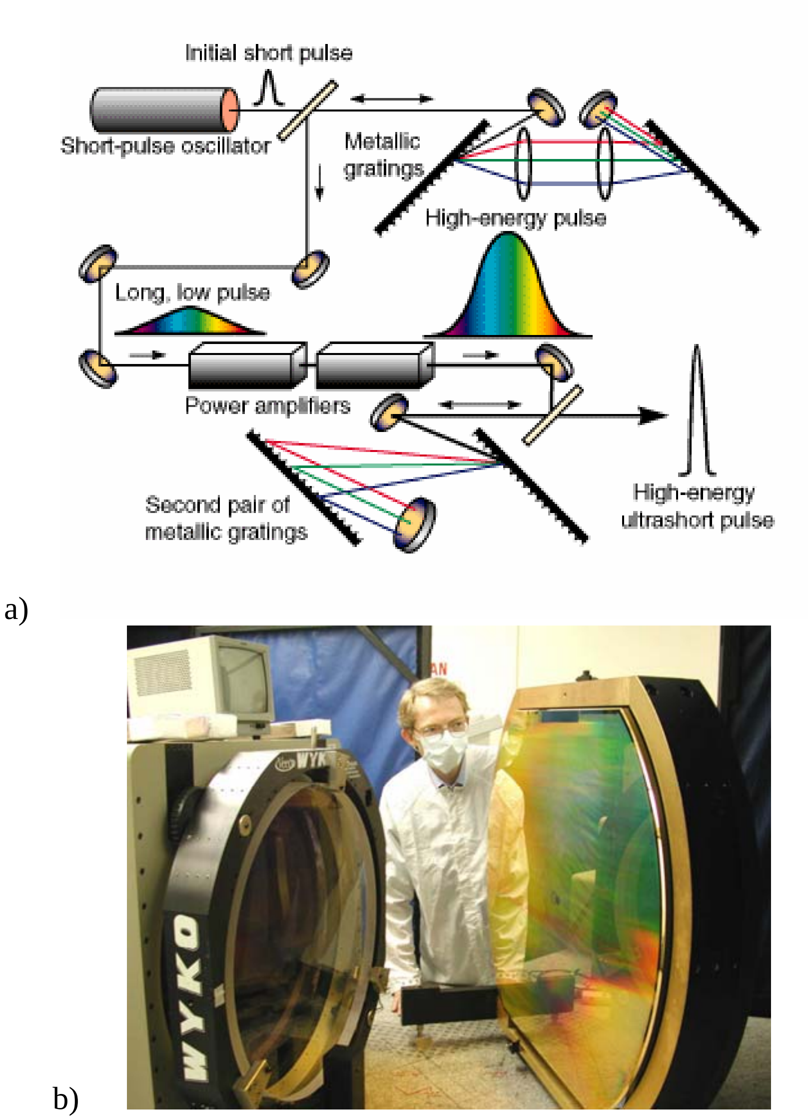

Figure 1.1: a) Diagram showing CPA scheme [3] and b) compressor grating from the PW CPA laser system at the Central Laser Facility at the Rutherford Appleton Laboratory, UK [4].

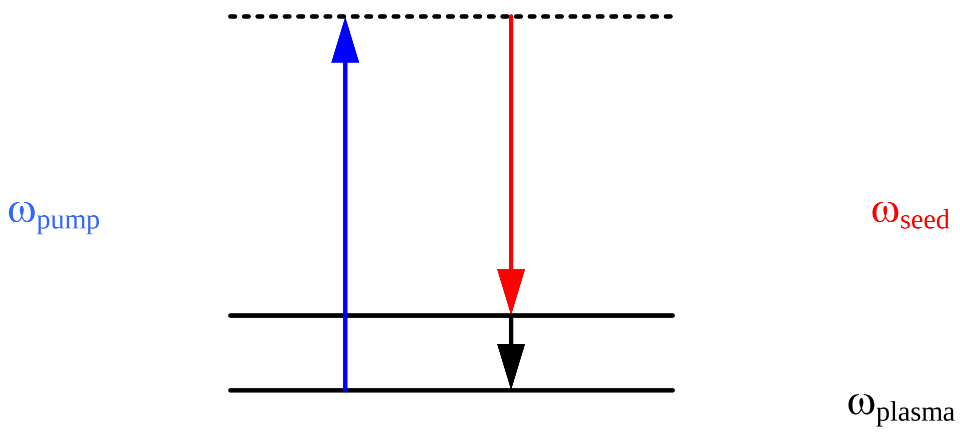

Figure 1.2: Illustration of the frequency requirements which need to be met for resonant RBS amplification.

demands on producing these gratings [5] place a final cap on CPA's effectiveness at extremely high powers (see Fig. 1.1 b)

1.2 Stimulated Raman Backscattering Amplification

In order to proceed with the amplification of ultrashort pulse lasers beyond the boundaries of CPA, altogether new schemes have been proposed. The central idea behind these new schemes is to utilize plasma as the medium which facilitates the amplification process. The reason that plasma is an ideal medium for producing the amplification and final compression of the pulse stems from the fact that plasma, by definition, is a gas which has already been completely broken down at an atomic level into its constituent ions and electrons. This allows the plasma to bear both the high power densities as well as the heat loads involved in the final compression of the amplified pulse. Additionally, fresh plasma can be produced each time the pulse is amplified thereby lengthening the effective lifetime of the setup as well as producing more uniform, reliable results.

Several coupling techniques, including Compton scattering, resonant Raman backscattering, and Raman backscattering at an ionization front, have been proposed. In the basic scheme for the use of plasma as an amplification medium, a long, relatively low intensity 'pump' laser pulse loses its energy to a short, high intensity 'seed' pulse with the plasma acting as a coupling medium. An important feature of stimulated RBS is that the pumped pulse grows to intensities much higher than that of the pump because the pulse continually encounters unperturbed regions of the medium and absorbs new regions of the pumping beam. The pumped pulse, in the absence of medium excitations, cannot return energy back to the higher-frequency pump (although it is more intense than the pump) and thus exits the interaction medium with a much larger intensity [6]. In order to circumvent the numerous possible instabilities related to waves in plasma (for example modulation instability resulting in laser filamentation), it has been shown that a resonant Raman backscattering regime can provide an amplification process which occurs quickly enough to outrun the instabilities [7]. It is with this resonant RBS scheme that Suckewer *et al*. have already demonstrated appreciable amplification of an incoming, ultrashort seed pulse [8] (see Chapter 1.3).

In the three-wave process of resonant RBS, the incoming EM pump and seed pulses excite the plasma and enable the transfer of energy from the pump to the seed pulse (see Fig. 1.3). This amplification occurs when the frequency difference between the incoming counterpropogating waves is exactly the plasma frequency:

$$\omega_{pump} - \omega_{seed} = \omega_{plasma} \;,\;\; \vec{k}_{pump} - \vec{k}_{seed} = \vec{k}_{plasma} \qquad 1.1$$

where $\omega_{plasma} = \sqrt{4\pi e^2 n_e / m}$ is the plasma frequency (see Fig. 1.2). This relationship, while being derived by taking into consideration a number of complex effects, can be intuitively seen as expressions of the conservation of energy and momentum in the three-wave process. Considering that the resonant RBS scheme is a three-wave interaction, it is sensitive to the plasma frequency and, thus, the electron density n_e. It has been shown that, for a backscattered beam with bandwidth $\Delta\omega_{seed} \approx 2\gamma$ where $\gamma = a_{pump}(\omega_{pump}\omega_{plasma} / 4)^2$ is the RBS growth rate and a_{pump} and ω_{pump} are the amplitude and frequency of the pump pulse respectively [9]. Assuming a monochromatic pump beam, the maximal nonuniformity of the plasma density determined by the resonance condition

$$\frac{\Delta n_e}{n_e} \approx 4\frac{\gamma}{\omega_{pump} - \omega_{seed}} \qquad 1.2$$

must be less than a few percent for amplification [10]. For a pump pulse with a wavelength of 800 nm and a seed pulse between 840 and 940 nm, a plasma density in the range of 0.4 – 3.8 × 10^{19} cm^{-3} is required. If the aforementioned conditions on the pump, seed, and plasma are met, the energy transfer from the pump to seed pulse can theoretically reach an efficiency of 90% [11].

Additionally, the amplification grows as $K = \exp(2\gamma L / c)$ where L is the length of the uniform plasma channel and c is the speed of light. The pump length should be twice the plasma length so that the pump pulse may traverse the plasma before encountering the seed pulse, and so that the amplified seed pulse may exit the plasma as the tail of the pump pulse leaves. Thus, it can be seen that a long, uniform plasma channel is necessary for implementation of the RBS amplification scheme.

The process of resonant RBS amplification can be divided into a linear and nonlinear regime. In the linear regime, the pump depletion is negligible, and the seed pulse is amplified and expanded in time. In the nonlinear regime (also called the π-pulse regime), the seed pulse is amplified and temporally compressed while continuing to remain stable and focused as it leaves the plasma. This effect is due to the fact that, as opposed to the linear regime, the pump pulse is strongly depleted by the seed pulse in the

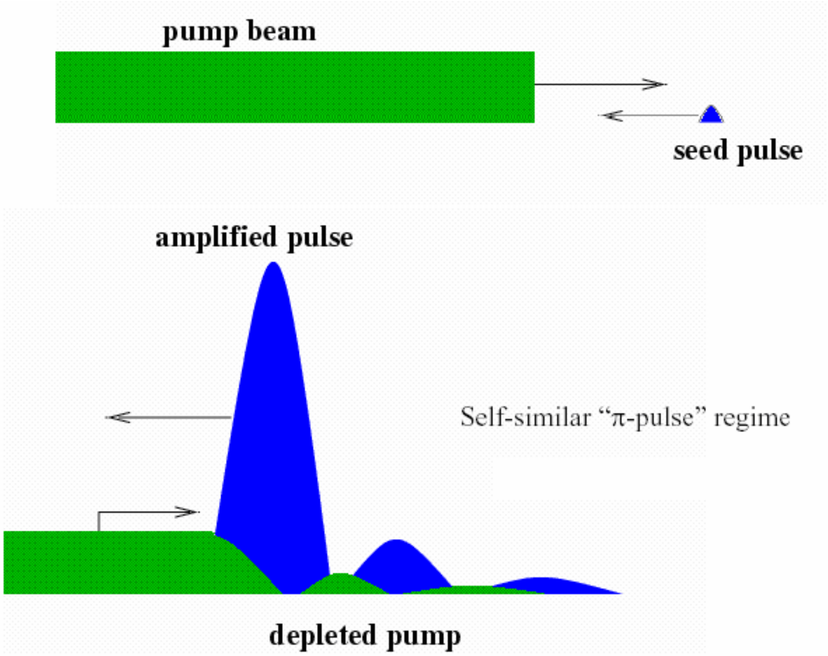

Figure 1.3: Amplification of the seed pulse via the three wave resonant RBS scheme [12].

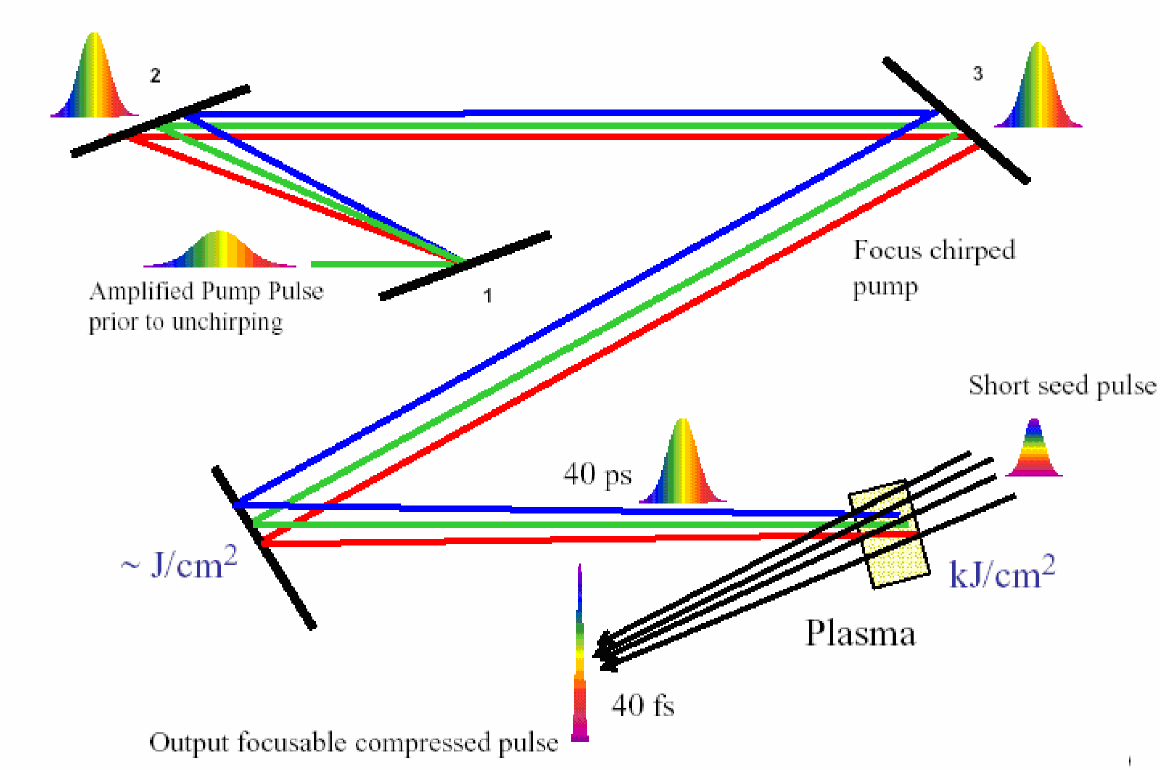

Figure 1.4: Illustration of the use of plasma as the coupling medium for the compression and further amplification of short pulses [12].

nonlinear regime. The front of the seed pulse is amplified through interactions with the full pump while the seed tail interacts only with the depleted pump (see Fig. 1.3), thus resulting in pulse compression.

Overall, the plasma involved in the RBS amplification scheme plays a very different role than the original solid state compression gratings within the original architecture of CPA. As illustrated in Figure 1.4, the chirped pulse is used as a means to an end rather than being the final product – it acts as the pump pulse which, along with the plasma channel’s coupling, serves to produce a short, highly amplified seed pulse. The nonlinear regime thus allows for the amplification and compression of ultrashort pulses with intensities on the order of 10^{20} – 10^{21} W/cm^2 to be reached economically and on the university scale.

1.3 Methods of Plasma Production for RBS Amplification

Several different setups have been used in an attempt to generate the plasma necessary to satisfy the RBS plasma conditions. One technique used to study the RBS amplification relies on creating a high-density plasma within a microcapillary. In this setup, a laser passes through a microcapillary tube and creates plasma either through ionization of the gas or through ablation of the surface material. With this method, amplification on the order of 10 has been demonstrated [13]. However, because the plasma is contained within the microcapillary, this setup makes plasma diagnostics difficult. Often, direct plasma measurements are not possible and indirect methods must be employed in order to extract the relevant information.

A second technique currently being employed uses gas jet plasmas as the amplification medium [15]. Already, Suckewer *et al.* have demonstrated energy amplification of approximately 100 with the use of a 2 mm long gas jet plasma (effective interaction length of 1-1.5mm) [11]. In addition to the energy amplification of the seed, even more recent work has been done to demonstrate the temporal compression of the seed pulse in the nonlinear RBS regime [8]. The main limitations of this technique, though, stem from the fact that an axially uniform plasma with length of greater than 2 mm is technically difficult to obtain due to the nonuniform laser energies deposited into the gas jet as well as the flow nozzles used. So far, a uniform channel exceeding this length has not been demonstrated. The traditional method of generating such a plasma has been to pass an ionizing laser pulse through a gas jet thus ionizing the gas and creating a plasma. Unfortunately, the nonuniformities in the gas jet (due to turbulent flow at the nozzle) give rise to a plasma with a varying density at longer plasma lengths and, therefore, a non-homogenous plasma frequency. While such a method has been able to produce the desired plasma frequency at limited ranges (thus allowing for verification of the applicability of the RBS method for laser pulse amplification and compression), a plasma with the desired density uniformly distributed throughout a longer length is necessary for further increasing amplification and compression. Limitations on the length of the plasma channel thus impose constraints on the maximum effective length of the pumping pulse because the pump and seed pulse can only interact within the plasma channel region. These constraints, therefore, limit the amount of energy which can be imparted to the seed pulse thereby limiting the amplification and compression process as a whole.

In addition to the work being done at Princeton University, other groups at various universities and national labs are carrying out related research. Groups at the Princeton Plasma Physics Lab (PPPL) are involved both in modeling and in the theoretical calculations for the resonant RBS scheme as well as other schemes of amplification. Over a decade ago, Augst *et al.* [15] used a laser-induced plasma in a backfilled container (thereby ensuring constant gas pressure) to study the tunneling ionization processes of noble gases at the University of Rochester. More recently, Gaul *et al.* [15] at the University of Texas have conducted several experiments studying the production of fully ionized He plasma channels using a short laser pulse in conjunction with a pulsed high voltage source similar to the setup used in our experiment. While the intent of this group was to learn how to avoid entrance and exit effects which lead to laser modulation (which can distort intense fs pulses propagating through the channel and end regions) rather than to create a longer or perfectly uniform plasma, their results and methods give physical insight into the processes involved in the channel's formation. Also, Milchberg et al. at the University of Maryland have been involved over the last decade with modeling and research using different experimental setups to generate a long, uniform plasma channel and characterize its spatial and temporal evolution.

The study of plasma channel generation by laser ionization of a gas is an area which has generated much interest and work for more than a decade. The innovation in this experiment lies in an altogether new experimental setup which attempts to avoid some of the previously mentioned difficulties inherent in other methods of plasma production. In order to work with a gas of uniform density, this experiment uses, essentially, a quiet gas maintained at a constant pressure inside of a small gas cell. With this setup, the previously mentioned difficulties and problems inherent in the microcapillary and gas-jet plasmas are avoided while allowing for the generation of a uniform plasma column with a density applicable to the RBS amplification regime (n_e ~ 10^{19} particles/cm^3). The issues involved with the microcapillary are somewhat resolved due to the fact that, because the volume of the gas cell is much larger than the microcapillary, the choice of material and surface effects are reduced. Also, the gas cell is designed so that a diagnostic interferometer can be constructed allowing for direct measurements of the plasma channel density. The problems related to flow nonuniformities in the gas jet method are an additional motivation for the gas cell method and are alleviated through using a quiet, uniform gas in this setup. Thus, as opposed to the backfill methods used by Gaul and Milchberg which require the beam to pass through gas rather than vacuum before arriving at the plasma, the setup used in our experiment is designed specifically for use in the resonant RBS scheme to produce a longer, more uniform plasma channel.

Chapter 2

Experimental Setup

The setup used in this project has evolved over the course of the experiment and is tailored for compatibility with the resonant RBS process. In the field of laser and plasma physics, everything from the characteristics of the laser and particulars of the optical setup to the geometry and materials used to contain the ionized gas is crucial to the experiment itself. While this experiment initially follows in the footsteps of others already successfully performed, the particular experimental setup and circumstances of the plasma production make this experiment and its results unique. Thus, in this section I will discuss the laser and optics setup used, the gas cell and vacuum chamber where the plasma is created, the electrical configuration used to investigate plasma formation with a preionized channel, and, finally, the diagnostic and data acquisition setup.

2.1 Laser System and Optics

The laser being used both for providing the ionizing pulse as well as the diagnostic interferometry pulse is a 1064 nm Lumonics Nd:Glass laser system (see Fig. 2.1 a). The laser system begins in the initial optical cavity with flash lamps triggered at 1 Hz pumping the active medium which lazes in the 1064 nm range. The pulse is then expanded by a telescoping lens and mode-locked by a Q-switched Pockels cell (an element which allows only certain polarizations through when a certain voltage is applied) and an acoustic modulator timed by the master oscillator to produce an extremely short pulse with a more precise single frequency. The resulting pulse consists of a train of 100 ps pulses which pass through a partial mirror and escape the cavity. A pulse selector is then used to slice the train so that only a specified number of pulses continue on (in this experiment, only a single pulse is used per shot). The pulse is then focused through a pinhole for purposes of pulse shaping (the wings of the pulse are abruptly cut) and then through a Gaussian filter to again smooth the wings to maintain a Gaussian pulse. Once the pulse has been spatially shaped, it passes through an amplifier which is protected by a Faraday rotator and several wave plates in order to ensure that the amplified pulse will not be reflected and damage the optics in the beginning of the laser system.

After being amplified, the pulse passes through a nonlinear potassium dihydrogenphosphate (KDP) crystal in order to produce the 532 nm second harmonic. Generating this second harmonic beam is not a trivial task – the process relies on the anisotropy of the KDP crystal giving rise to its optical birefringence, where the material's refractive index depends not only on the incoming beam's wavelength, but also on the polarization direction of the electric field vector with respect to the crystal. The crystal's polarization can thus be described in a Taylor series expansion as

$$\mathrm{P}_1 = \varepsilon_0\, \chi^{(1)}\, \mathrm{E}_1 + \varepsilon_0\, \chi^{(2)}\, \mathrm{E}_1^2 + \varepsilon_0\, \chi^{(3)}\, \mathrm{E}_1^3 + \ldots\ldots\ldots \qquad 2.1$$

where the anisotropy allows for a non-zero second order correction term to the crystal's electric polarizability producing three-wave mixing and the generation of higher harmonics. The incoming beam's intensity (I_1) is related to the second harmonic produced (I_2) as

$$I_2 \propto l^2 \sin c^2 (1/2\,\Delta k l) \qquad 2.2$$

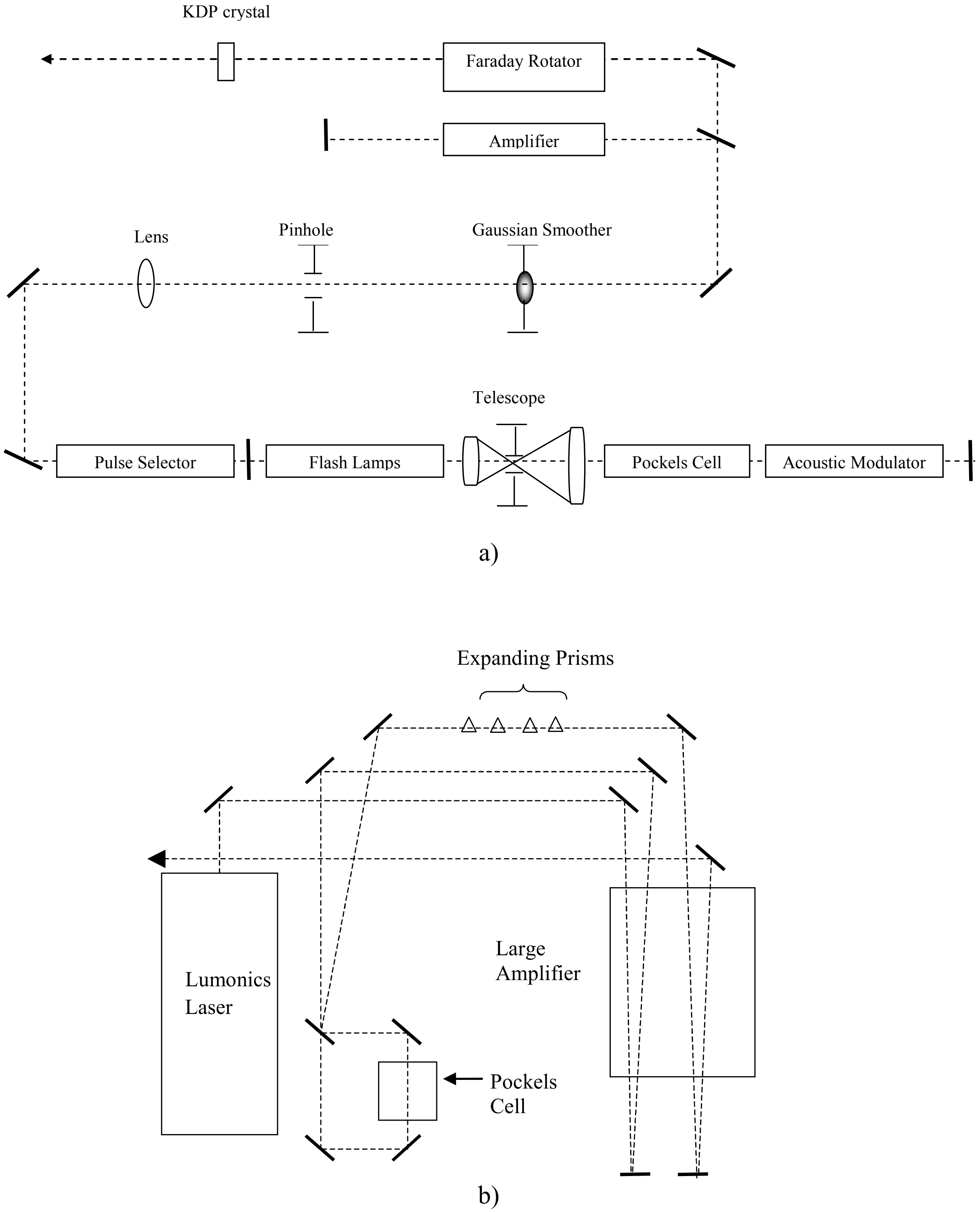

Figure 2.1: a) Lumonics laser system for the generation of the ionizing and diagnostic beams and b) the amplification system for the ionizing beam.

where l is the length the beam passes through the crystal and $\Delta k = k_2 - 2k_1$ is the mismatch parameter relating the wave numbers of the incoming and outgoing beams.

Thus, while higher harmonics are generated at a range of incident intensities and angles, it is the second harmonic which is most easily produced (due to its only being multiplied by a small χ^2 term). Specifically, when $\Delta k = 0$, phase matching is said to occur and the second harmonic is optimally produced resulting in the production of a $\lambda_2 = \frac{1}{2}\lambda_1$ beam [17]. Thus, the polarization of the beam exiting the Faraday rotator is oriented precisely with respect to a KDP crystal of correct length and geometry so that the 532 nm diagnostic beam is most efficiently produced.

Ultimately, a 100 ps 1064 nm pulse (or 'ionizing beam') with approximately 20 mJ energy along with a 532 nm pulse exit the laser system. As will be described next, the 1064 nm beam is used for creating the plasma while its second harmonic (532 nm) is used for diagnostic purposes.

2.1.1 Ionizing Beam Optical Setup

After exiting the laser, the beam passes through a beam splitter causing the 1064 nm black beam and the 532 nm green beam to diverge. The black beam then makes two passes through a large amplifier. This amplifier consists of a glass slab pumped by several flash lamps. The beam is reflected 15 times within the slab as it makes each pass through the amplifier so as to maximize its path length (and, therefore, energy gained)

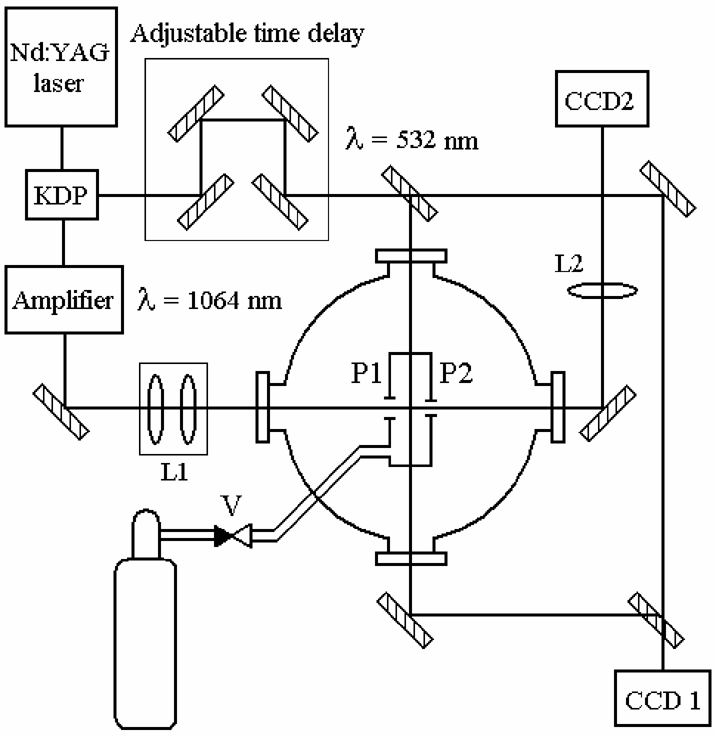

Figure 2.2: Experimental setup showing optical system, gas cell, and diagnostic system.

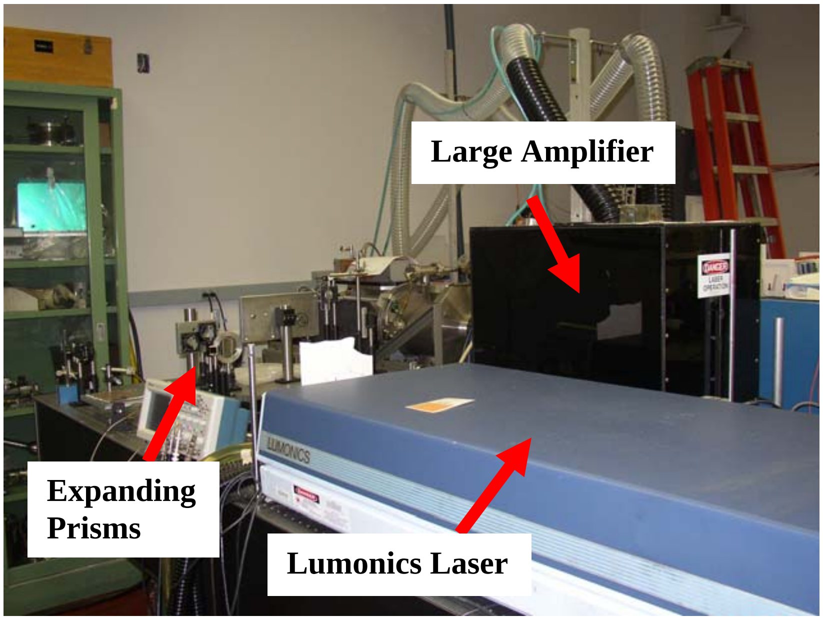

Figure 2.3: The Lumonics laser, expanding optics, and large amplifier are shown.

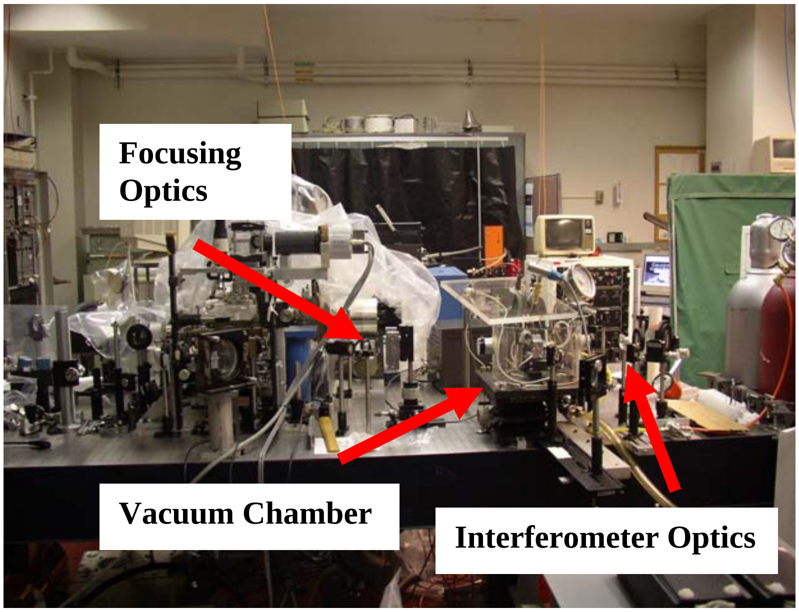

Figure 2.4: The focusing optics along with the interferometer setup and vacuum chamber are shown.

through the amplifier. Upon exiting the amplifier after its second pass, the beam is expanded via several prisms to a size of approximately 5 cm by 1 cm. The beam then passes through a Pockels cell in order to protect the sensitive optics in the laser and amplification setup from damage due to any portion of the ionizing pulse which may be reflected back along the optical path. The beam then makes two more passes through the amplifier and exits with a final energy of approximately 0.5 J. The beam is spatially stretched before making the final passes in order to avoid intensity-related damage to the final optics After being amplified to its final energy, the beam then exits the main laser room and enters the rest of the experimental setup (see Fig. 2.1 b and 2.3).

The rectangular 5 cm by 1 cm beam is then focused in order to increase its intensity (in order to ionize the gas) as well as to pass with minimal losses (due to the pinholes) into the gas cell. To this end, the beam passes through two cylindrical lenses which focus it in the vertical direction (see Fig 2.2 and 2.4). When the beam shape is a 1 cm by 1 cm square, it passes through another cylindrical lens (L1) which focuses the beam horizontally. These two sets of lenses must be carefully aligned so that the beam travels parallel to the table (in order to allow for easier alignment of the gas cell pinholes and the CCD camera – see Section 2.2) and so that the focal plane occurs inside the gas cell. The beam is focused to a 60 μm by 60 μm square (treated here as a circle with diameter 70 μm) and, while the focal plane of the beam was originally aligned to be approximately in the center of the gas cell, its position along the axis of the beam was iterated so as to produce the best plasma channel possible. Thus, for a diffraction limited beam of λ=1064 nm with a beam waist of ~35 μm, the Rayleigh length (Z_R) is 3.7 mm as defined by

$$Z_R = N \cdot \pi \cdot w^2 / \lambda \tag{2.3}$$

where w is the beam waist, λ is the wavelength of the beam, and N is the index of refraction of the medium ($N_{nitrogen}$=1.000297). Thus, the ionizing beam is most tightly focused for almost the entirety of the gas cell separation. The pulse which reaches the gas cell has a temporal length of approximately 100 ps and an energy of ~0.5 J resulting in an intensity on the order of 10^{14} W/cm^2.

2.1.2 Second Harmonic Optical Setup

After being split off from the main heating beam via a beam splitter placed directly after the laser, the second harmonic (532 nm) passes through an optical time delay. The time delay consists of two mirrors with one being fixed and the second free to move along a translational track in the direction of the beam's propagation (see Fig. 2.2). In this way, by varying the position of the second mirror, the time delay can be altered so the plasma may be probed at varying times after the arrival of the 1064 nm ionizing beam in order to get a complete picture of the temporal evolution of the resulting channel. After the time delay, the second harmonic beam arrives at the gas cell and acts as the probe beam of a Mach-Zender interferometer (see more about the diagnostic system and data collection setup in Section 2.4).

2.2 Gas Cell

The gas cell setup consists of an aluminum chamber placed on a precision mount and housed inside of a Plexiglas vacuum chamber. This vacuum chamber is 35 cm in diameter and has four windows oriented such that the ionizing beam may enter in one direction while the secondary harmonic beam may pass through perpendicular to the ionizing beam. The chamber is connected to a pump which can achieve a backpressure vacuum of approximately 600 mTorr (without gas inside the cell present) within the chamber, as well as a gas tank which can provide varying pressures of gas in the gas cell.

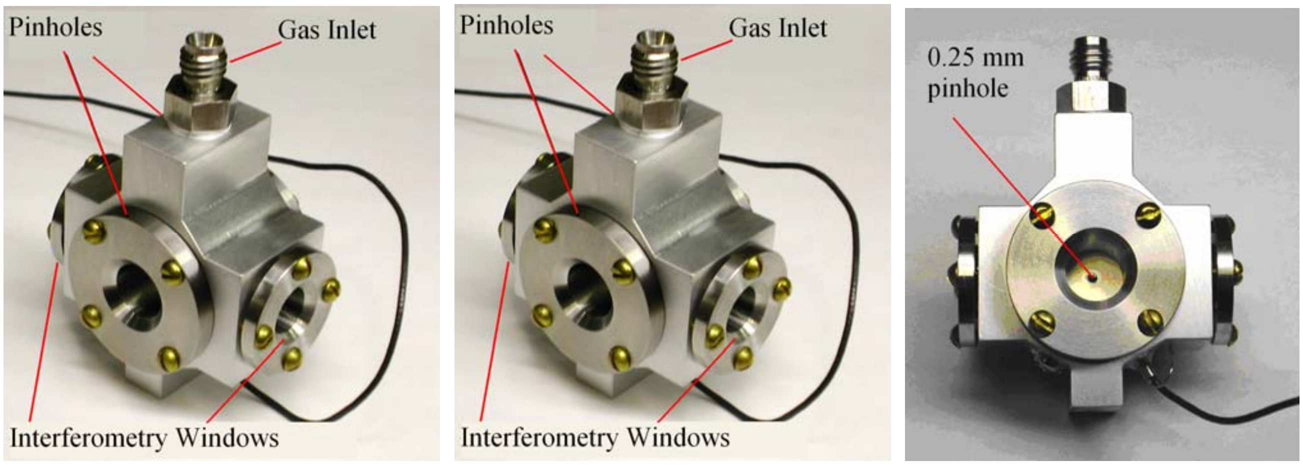

(a) (b) (c)

Figure 2.5: a) The gas cell is shown along with interferometery windows and gas inlet. b) The gap between the pinholes for channel formation is shown. c) The pinhole placement and size is shown.

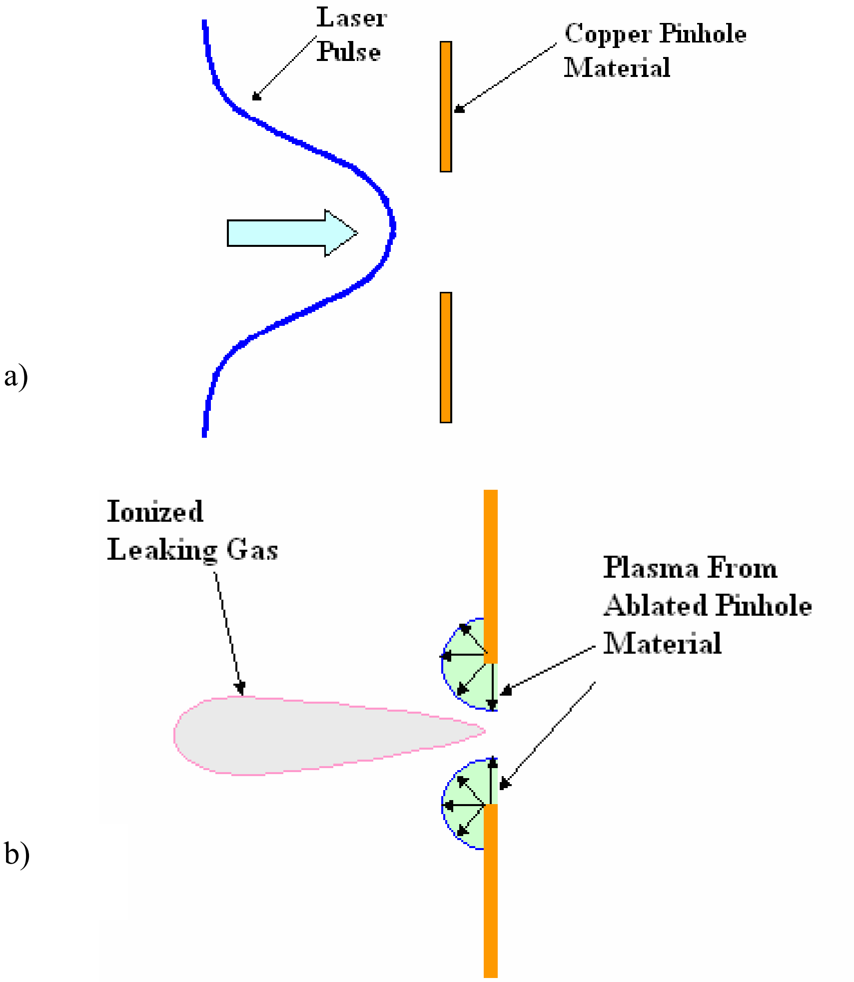

Figure 2.6: a) Shows the laser pulse with the majority of its energy focused inside the pinhole diameter but with the wings still able to interact with the pinholes. b) Deleterious plasma is formed in several locations in addition to inside the cell – gas leaking from the cell is ionized as well as some material being ablated from the pinhole.

Both a vibrational and mechanical pressure sensor were used to measure the pressure of the gas inside the cell as well as the backpressure in the chamber.

The gas cell is made of aluminum and is constructed so that the gas enters through the top of the cell (via a distributor made of porous metal to avoid pressure nonuniformities) and the pressure is measured at the bottom (see Fig. 2.5). Optical access to the plasma is provided by two windows which allow the second harmonic beam to probe the plasma channel perpendicular to its axis. In the main ionizing beam line, two copper pinholes (P1 and P2 in Fig 2.2) are used to keep the gas contained within the gas cell while still allowing the ionizing beam to pass. The diameter of the pinhole is roughly 250 μm at the beam's inlet and 150 μm at the exit. The sizes are designed so as to minimize the negative effects of ablation described in the next paragraph (requiring larger pinholes) while also minimizing pressure disturbances inside the gas cell (requiring smaller pinholes).

While the gas inside the cell is still much more uniform than in the case of the gas jet, several new problems arose in using the gas cell architecture. Because a laser with a spatial Gaussian profile of the form

$$I = I_0 \exp(-\frac{x^2 + y^2}{r^2}) \qquad 2.4$$

(where I_0 is the peak intensity, x and y are the coordinates from the center of the pulse and r is the beam size) with peak intensity ~10^{14} W/cm^2 is used to create a plasma with the desired density, it can be shown that an intensity on the order of 10^{12} W/cm^2 can still be found in the wings of the pulse (i.e. at a radius ~ 250 μm). This presents two potential problems. First, small amounts of gas escaping from the pinhole produced a very low density plasma along the direction of propagation of the laser (see Fig. 2.6).

Fortunately, this plasma was shown (via interferogram analysis) to absorb only very little energy from the main beam both because of the low density of the gas as well as the lower intensity of the beam in this region. Second, with such a large intensity incident on the surface of the pinhole material, the laser can produce ablation resulting in plasma formation on the outer gas cell wall, thus introducing shock waves into the cell. In addition to these shock waves possibly disrupting the gas density inside the cell, the pinhole may be effectively closed via the production of radially expanding optically thick plasma (see Fig. 2.6). While these issues posed considerable problems at the experiment's onset, careful focusing and alignment of the beams greatly improved the situation.

2.3 Electric Discharge Sources

In addition to using the main ionizing laser pulse as a source for ionization, the effects of using electrically induced DC glow discharges and pulsed AC discharges as methods of pre- and further ionization of the gas were also investigated. Two different electrical setups were used with each producing approximately the same final results. Both setups made use of a 2 kV DC source (with a max amperage of 1.6 mA) attached to the gas cell by connecting one of the copper pinholes to the positive voltage source and grounding the other pinhole. Both pinholes are attached to plastic flanges (which are screwed onto the aluminum gas cell with nylon screws), thus providing a means to electrically isolate each pinhole from one another. The 2 kV source allows for the production of a steady glow discharge between the entrance and exit pinhole with the dually intended purpose of helping to guide the laser pulse as it enters the plasma as well as producing seed electrons which can later be utilized to create an avalanche effect resulting in a denser plasma (see Fig. 2.8). Also, it was found that the pulsed source alone was unable to produce a breakdown in the gas cell without the DC glow already established. In the first electrical setup used, the 2kV source was connected to the pinhole via a 1 MΩ resistor both for limiting the DC current as well as protecting the DC source from damage due to the pulsed source (see Fig. 2.7 a). In the second setup, the DC voltage passes to the pinhole through several 1 kV diodes to ensure protection from back-currents without affecting the output of the source (see Fig. 2.7 b).

In addition to the DC source, a timed 20 kV AC pulse was used in order to further ionize the gas. The pulse produced is approximately 100 ns in length (much longer than the laser pulse) with a peak current on the order of 100 A. The method of temporally aligning the discharge with the arrival of the ionizing beam was the same in both cases. The timing for the laser/amplifier system is controlled by the master timer which consists of a clock which runs into a Stanford timer. One of the outputs from this timer was then run into a second Stanford timer and was used to trigger the capacitor discharge of the 20 kV pulser. In order to determine the relative arrival of the ionizing beam with the pulsed discharge, a photodiode (with 25 ns resolution) was placed at the entrance to the vacuum chamber and was triggered by the same signal which triggered the pulsed discharge. Additionally, a Rogowski coil, placed directly prior to the vacuum chamber, was used to determine the arrival of the signal from the pulsed discharge source. The delay on the pulsed source was then appropriately adjusted so that the arrivals of the ionizing beam and electrical discharge were coincident.

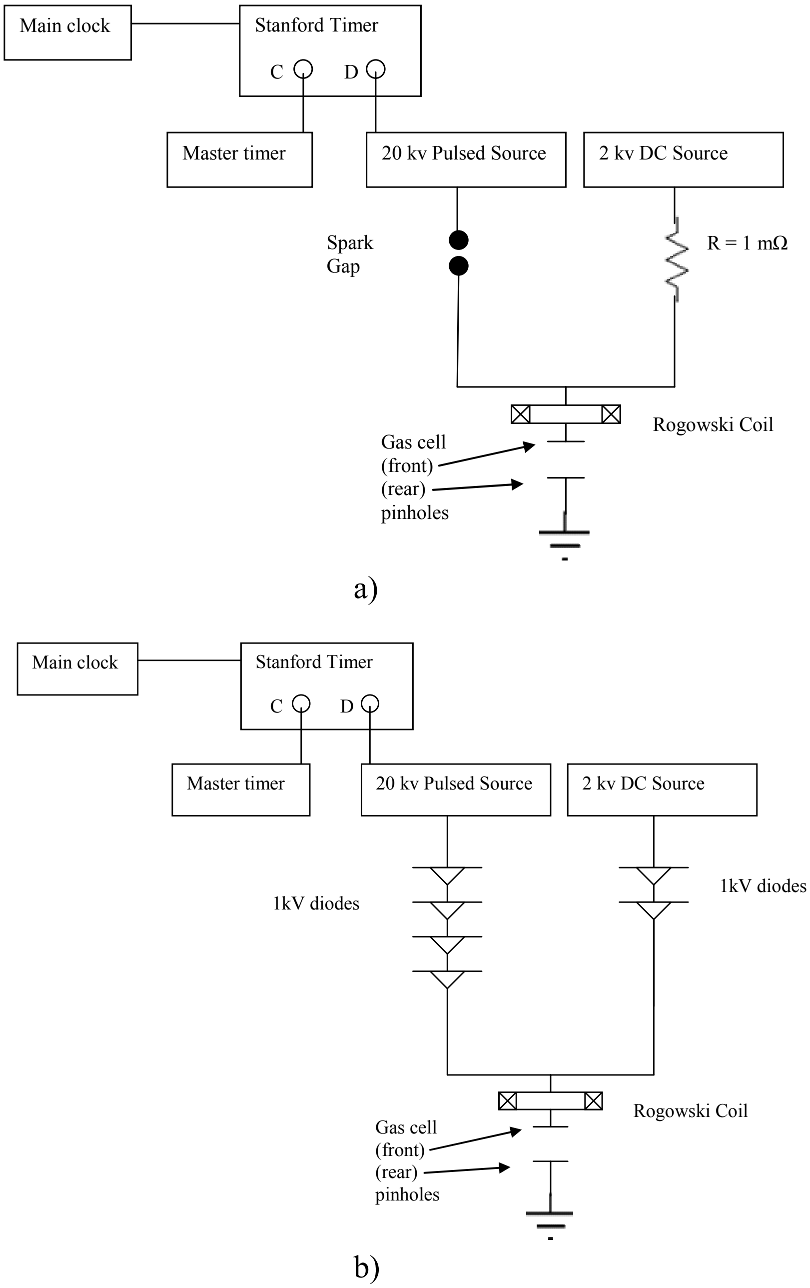

Figure 2.7: a) 1st and b) 2nd electrical setup for pulsed and DC discharge sources.

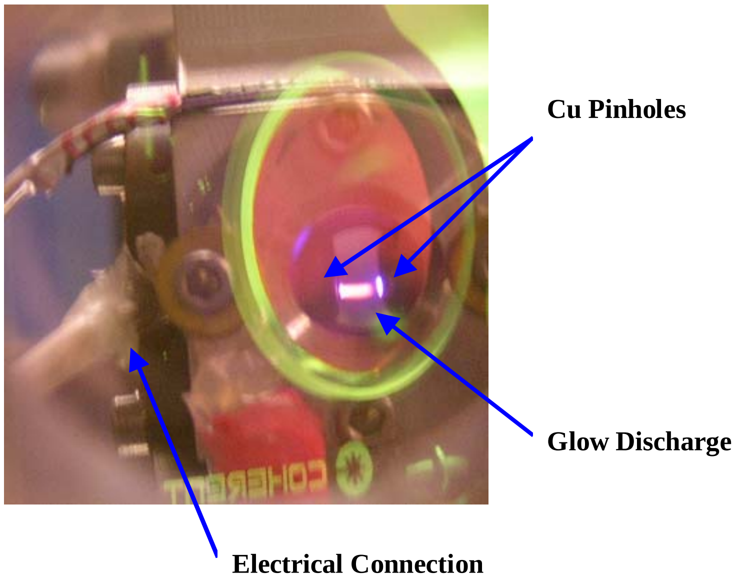

Figure 2.8: Picture showing the electrical connections to the pinhole as well as the DC glow discharge produced.

In the first electrical scheme, the output of the pulser was connected to an open air spark gap to insulate the system from any damage which may result from current flowing while the DC source is connected in series with the plasma channel. When the pulser fires, the air in the spark gap is broken down and current flows from the pulser, through a resistor, where it is connected to the output of the DC source. In the second electrical setup, the output from the pulsed source passes through several 1 kV diodes directly to the output of the DC source. In both cases, the signal then passes through a 0.1 V/A Rogowski coil which is then connected to a 50 Ω load and is used to measure the output current of the pulser in addition to, as was previously mentioned, being used for purposes of timing. Finally, the output of the pulser is connected to the pinholes. Coaxial cables were used to transmit the pulses, and the entire electrical circuitry was placed inside of an insulating box for noise reduction.

This pulsed electrical discharge setup is similar to that used by Gaul *et al.* [15] in that it makes use of a pulsed high voltage source to create a plasma spark. In that experiment, though, two knife-edge electrodes are physically immersed in a large container with higher backfilled pressures to produce the plasma. Thus, our setup differs in our use of a small volume of gas as well as the fact that our electrodes (the pinholes) are in contact with vacuum on the outside rather than gas of the same density. Finally, it is important to note that it would be extremely challenging to strike a stable, cylindrical discharge close to the nozzle in a gas jet setup, due to the typical metallic components found in the nozzles as well as the fact that the flowing gas is not uniform and would most likely result in the bending of the discharge. Thus, as the laser pulse must pass through this discharge, it is evident that an arced discharge would have negative effects and further demonstrates the advantage of working with a quiet, uniform gas.

2.4 Diagnostic System

The diagnostic and data acquisition system are designed to probe and record information about both the plasma channel and the laser pulse. Schematically, the diagnostic system consists of several components to measure the ionizing pulse energy, an interferometer to measure the plasma density, and several cameras to record and transmit the information to the computer for storage and processing.

Prior to my arrival, a several nanosecond pulse was used in the interferometer setup to image the plasma. Because the formation and evolution of the channel occur on the order of 100 ps, though, this setup was unable to properly image the channel with acceptable resolution. Rather than seeing a coherent plasma channel, all that was seen was the slowly expanding shock waves which remain after the channel has disappeared (see Fig. 2.9 a). In order to move to shorter times scales, the split off second harmonic of the main heating beam is used as part of the interferometer system. In this way, the temporal resolution of the probing beam is on the same order as the ionizing beam and the phases of the beams are well known. The split off probe beam then runs through an optical time delay and before passing through the plasma (perpendicular to its axis) as part of a Mach-Zender interferometer. The result of this diagnostic is an interferogram which allows for the determination of the density and distribution of the produced plasma channel at a range of times after the plasma is produced (see Fig. 2.9 b).

Two charge coupled device (CCD) cameras are placed at the ends of the optical paths of both the ionizing and probe beams and are connected, via a television, to a computer. The CCD camera in the ionizing beam line (CCD2 in Fig. 2.2) is used, in conjunction with the television monitor, only for aligning the ionizing beam and determining its shape and approximate dimensions. For the second harmonic probe beam, the interferometer is adjusted (along with supplementary optics) so that the center of the gas cell is imaged at the corresponding CCD camera (CCD1 in Fig. 2.2). The output of the CCD is connected to a television monitor so that the interferometer can be more easily aligned and the fringe spacing and angle can be adjusted.

This signal is then sent to a computer for storage and processing. A framegrabber code written by Dr. Dunaevsky is used to take and store the interferometer image. Immediately prior to the laser firing, the code must be manually triggered to begin recording data. It then records 100 images taken over a 3 second time interval. Only one frame actually contains the interferometer signal, and a computer code is used to ignore all uninformative images and save only true data. Due to noise in the system (caused by the high current pulsed source and spark produced within the gas cell), I was required to modify the code by editing the conditions necessary for selecting the correct image frame so that spurious signals would not be stored instead of real images. Additionally, because the resulting image from the framegrabber program is the result of two interlaced semiframes (with one being the true image and the other being simply black), the image has horizontal black lines in every other row. A short program (see Appendix A) was written to remove these lines by averaging adjacent rows in order to improve the analysis of the images.

In addition to the plasma diagnostic and analysis apparatus, the status of the laser itself is monitored upon each output pulse. The output of two photodiodes (one placed inside the laser with another monitoring the laser's output) are connected to an oscilloscope. Also, the pulse shape and timing of the Pockel's cell is monitored via the oscilloscope, with all of the previously mentioned signals on the same oscilloscope being triggered by the falling edge of the pulsed AC signal. Thus, the relative origins, durations, and amplitudes of each signal are known for each shot. Also, a pellicle (5% reflectance) is used to reflect a small portion of the ionizing beam prior to the its entering the vacuum chamber. This reflected beam is directed to a Gentec Ed-200 energy meter (0.901 J/V) which outputs the result to a separate oscilloscope so that the input energy to the gas cell can be monitored on a shot by shot basis. A second energy meter (a Gentec

QE-25 with attenuator – 0.3 J/V) is placed after the vacuum chamber so that the amount of energy lost as the pulse passes through the gas cell can also be quantified.

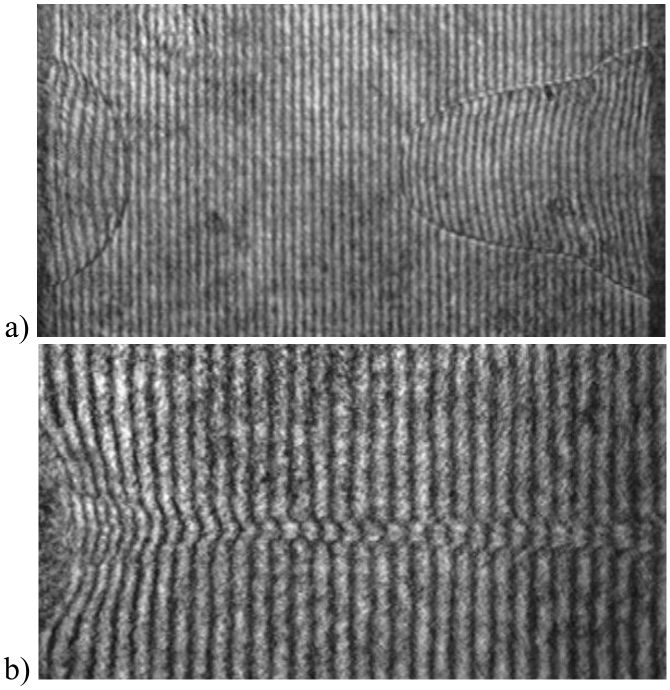

Figure 2.9: Interferogram made after a) 400 ns and b) 900 ps in N_2.

Chapter 3

Data Analysis

Analysis methods for interferometry are well established and include a variety of different techniques. In this section, I will describe two techniques commonly used for interferogram analysis: the Fast Fourier Transform (FFT) technique for ineterferogram analysis and density profile analysis using Abel inversion. Also, I will discuss their application to the calculations and analysis used in this experiment.

3.1 FFT Interferogram Analysis

To produce an interferogram, two beams of light (one typically designated as a probe beam (E_1) and the other as a reference beam (E_2)) are split from one another and travel different optical paths before meeting up again at a common location. When the two beams meet, they typically have some resulting angle between their directions of propagation as well as a phase shift (see figure 3.1 a) [18]. The resulting intensity of the interaction of the two beams is $I(x,y) = \langle (E_1 + E_2)^2 \rangle \big|_t$ which, after being written in terms of new amplitudes, can be defined as

$$I(x,y) = A(x,y) + B(x,y) \cdot \cos(2\pi u_0 x + \Phi(x,y)) =$$

$$A(x,y) + C(x,y) \cdot \exp(j2\pi u_0 x) + C^*(x,y) \cdot \exp(-j2\pi u_0 x) \qquad 3.1$$

where u_0 is the spatial carrier frequency of the interference pattern, $A(x, y)$ represents the low-frequency background intensity, $B(x, y)$ is the local fringe visibility, $\Phi(x, y)$ is the local fringe phase and $C(x, y) = 1/2 \cdot B(x, y) \cdot \exp(j\Phi(x, y))$.

In order to extract phase information about the object of interest from the resulting interferogram, the Fourier transform method proposed by Takeda et al [19] (or some variation thereof) is often used. The desired phase information ($\Phi(x,y)$) corresponding to the information stored within the probe beam is contained in the $C(x,y)$ term of Equation 3.1. Thus, the problem becomes one of extracting the $C(x,y)$ term from the $I(x,y)$ intensity equation above. By taking the Fourier transform of the intensity, it can be seen that the intensity

$$i(x, y) = a(u, v) + c(u - u_0, v) + c^*(u + u_0, v) \qquad 3.2$$

is represented as two peaked functions in the Fourier transform plane (see Fig. 3.1 c). The center lobe (defined by $a(u,v)$) represents the undisturbed, background phase frequency of the interferogram while the left and right lobes (defined by $c(u\text{-}u_0,v)$ and $c^*(u+u_0,v)$ respectively) contain the desired phase shift information. Through band-pass filtering the image (thereby eliminating the low frequency background) and keeping only the phase shift information (c orc^*), Φ(x,y) can be calculated by taking the complex logarithm of $C(x,y)$ yielding

$$\log[C(x, y)] = \log(1/2\, B(x, y)] + \log(\Phi(x, y)] \qquad 3.3$$

Thus, the phase distribution is determined (modulo 2π) and must be properly unwrapped (to rid the distribution of artificial 2π phase jumps) before yielding complete results [20]. The final product is a continuous phase distribution which, in the case of plasma diagnostics, gives information about the plasma density and, indirectly, the frequency of the plasma.

In order to analyze the interferograms produced in this experiment, I wrote a program which performs the previously mentioned calculations and returns a phase distribution. Unfortunately, two problems inhibited the effective use of this program. First, the quality of the interferograms produced (related to the noise from the CCD camera and processing of the image as well as the inhomogeneities of intensity of the diagnostic beam) made using such a technique very difficult without employing more complicated corrections.   Second, this method has a difficult time dealing with the particular shape of the fringe shifts in this experiment. Not only did the phase shift very rapidly, but the plasma was dense enough in many regions to produce fringes which shifted by more than 2π (thus crossing and mixing with other fringes). These problems also made the results produced by another program (using the same methodology) generally unreliable.

Ultimately, I evaluated the phase distribution along the axis of the channel by hand. First, in order to calibrate length scales in the interferograms, an interferogram of a piece of wire with known dimensions was made. ImageJ, a java application, was then used to reduce noise and increase contrast so that the fringes could be more easily identified and quantified. I measured the lengths, diameters, and phase shifts for each fringe by counting the number of pixels related to the corresponding dimension.

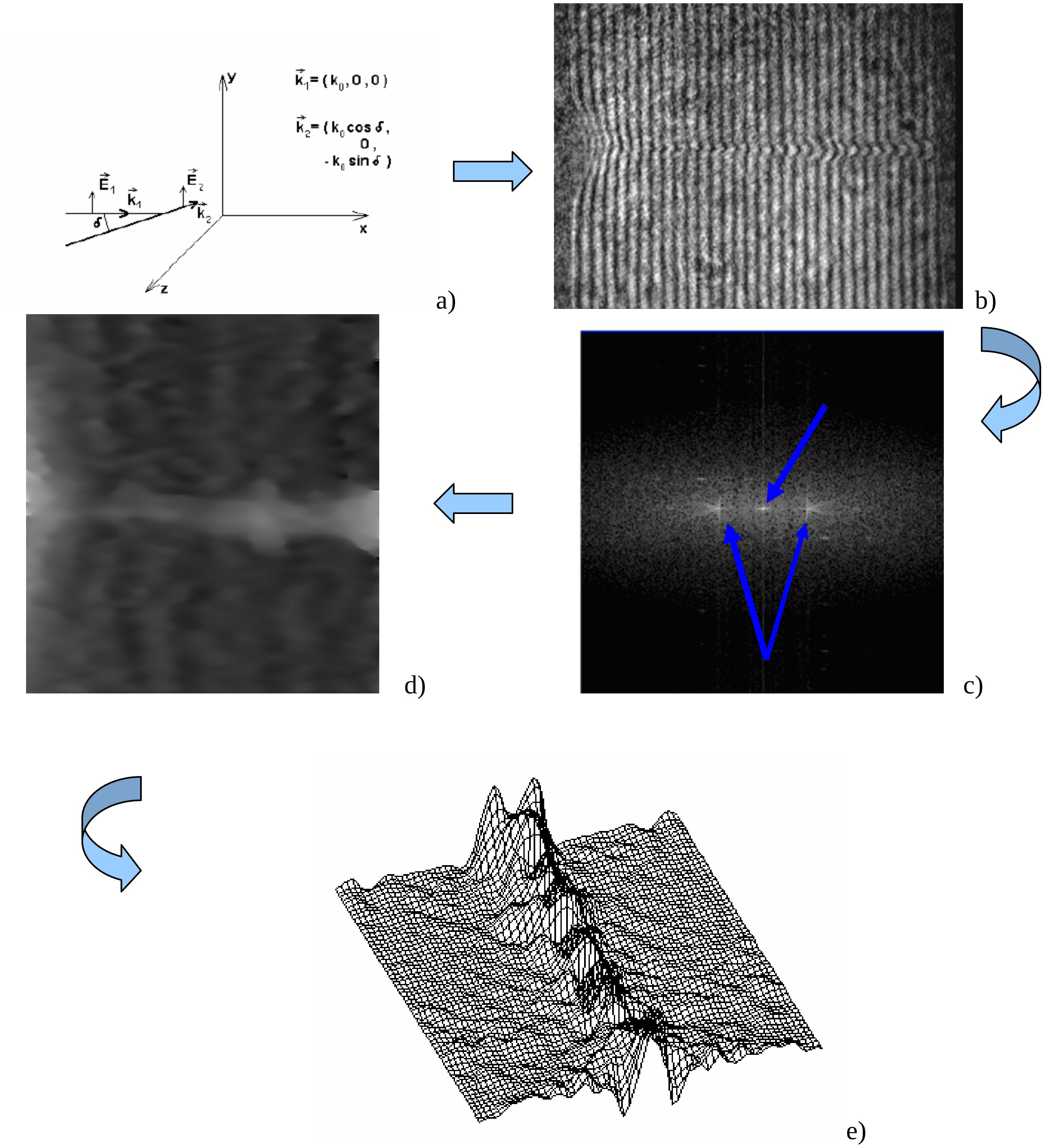

Figure 3.1: The creation and processing of interferograms via the FFT analysis method. a) First, the two beams interfere b) to produce the interferogram. c) The Fourier transform of the interferogram is shown with the left and right lobes carrying the disturbance information and the central lobe carrying the background frequency information. d) A 2D greyscale density map is then produced and then e) rendered in 3D (via Abel inversion) to illustrate the channel dimensions and density.

These values, in units of pixels, were then converted to real lengths and the densities were estimated by relating them to the observed fringe phase shift assuming cylindrical symmetry and uniform density.

3.2 Density Profile Analysis Using Abel Inversion

In order to extract the radial distribution of the desired object, the analysis of individual fringe shifts using Abel inversion was used. In the scenario described in the previous section, the probe beam first passes through the object of interest before interfering with the reference beam (see Fig. 3.2). For a plasma with electron density n_e, its index of refraction is defined as

$$N = \sqrt{1 - \frac{n_e}{n_{cr}}} \tag{3.4}$$

where n_{cr} is the critical density of the plasma (a 532 nm beam cannot propagate in regions in which the $n_{cr} > 3.9\text{x}10^{21}$ cm^{-3} [21]). The difference between the Abel inversion method and the estimation method previously described is that the estimation assumes a particular uniformity and geometry of the plasma (leading to a direct relationship between the index of refraction and number of fringe shifts) while Abel inversion extracts details of the object's density profile for arbitrary geometries and anisotropies. Thus, the assumption of cylindrical symmetry is maintained in this method (for this experiment) but the assumption of uniform density along the path length is dropped. The interferogram is simply a map of fringe shifts described by

$$\Delta\varphi(y) = 2\frac{\pi}{\lambda}\int_{x_1}^{x_2}\left(\left(1 - \frac{n_e(r)}{n_{cr}}\right) - 1\right)dx \tag{3.5}$$

where x and r are defined in Figure 3.2. The goal is then to extract the electron density map from the interferogram via Abel inversion as defined by

$$h(y) = 2\int_{y}^{R} f(r)\frac{r}{\sqrt{r^2 - y^2}}dr \tag{3.6}$$

Because the interferogram is composed of discrete components and the computation is done numerically (rather than algebraically) for an arbitrary fringe shift, several methods have been proposed in order to avoid performing integration and taking derivatives of f (as in the case of the standard definition

$$f(r) = \frac{-1}{\pi}\int_{r}^{R}\frac{dh(y)}{dy}\frac{1}{\sqrt{y^2 - r^2}}dy \tag{3.7}$$

.

In particular, a method proposed by Pretzler and Naturforsch [22] employs a Fourier transform technique to perform the Abel inversion. In this method, f(r) is written as

$$f(r) = \sum_{n=N_l}^{N_h} A_n f_n(r) \tag{3.8}$$

where the $f_n(r)$ are written in a cosine expansion defined as

$$f_n(r) = 1 - (-1)^n \cos\left(\frac{n\pi r}{R}\right) \tag{3.9}$$

and the A_n are found by minimizing a least squares fit to the real data as defined by

$$\sum_{n=N_l}^{N_h} A_n \sum_{k=1}^{N}(h_n(y_k)h_m(y_k)) = \sum_{k=1}^{N}(h(y_k)h_m(y_k)) \tag{3.10}$$

Thus, complicated integration is replaced by easily calculated integrals whose expansion coefficients are simply proportional to the Fourier coefficients (another pre-tabulated set of integers). In this way, fringe analysis can be done quickly and efficiently (as long as attention is paid to setting the proper boundary conditions).

For analysis in this experiment, Dr. Dunaevsky wrote a code which I modified to perform the Abel inversion in order to study the radial distribution of the plasma (see Appendix B). The input to the program is a file containing a single fringe from the region of interest and the output is the radial density profile of the plasma. Because of the issues mentioned in the previous section regarding the quality of the interferograms, the interferograms needed to be modified before accurate results could be attained from the program. Again, I used ImageJ to isolate a single fringe and then appropriately adjust the contrast, identify the center of the channel and inter-fringe spacing, and smooth the intensity of the image so that the fringe became completely continuous (see Fig. 3.3). Once this process was complete, the program was used to extract the desired information.

3.3 Uncertainty Estimations

In order to estimate the uncertainty of the density calculations, the approximations made by Ping et al [23] were adopted. The methodology used assumes that there are three sources through which uncertainty enters into the density calculations -- the noise in the interferograms, the extraction of fringes, and the calculation of Abel inversion. The first two are estimated to be <10% altogether, whereas the Abel inversion could introduce

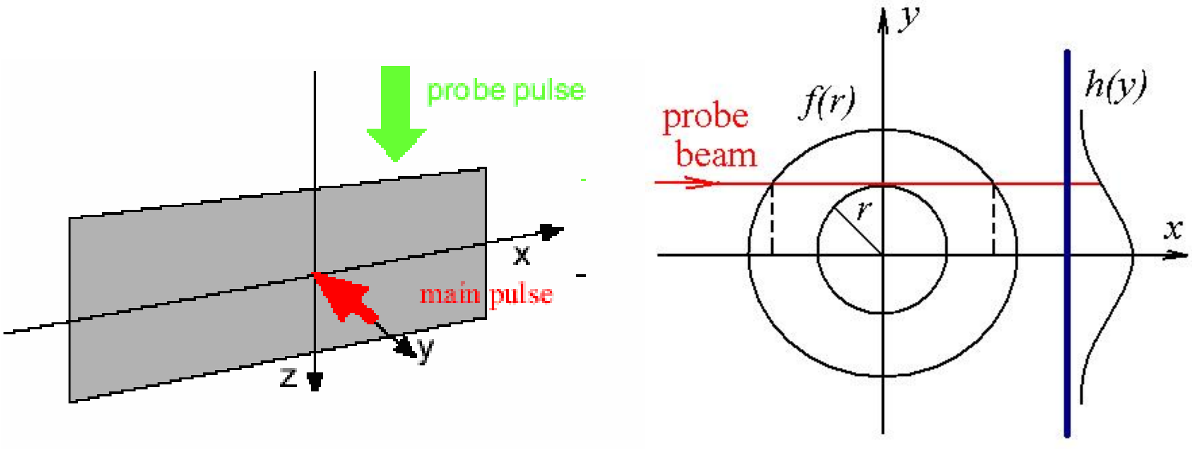

Figure 3.2: The probe beam is shown along with the position of a particular ray passing through a plasma channel with density n_e.

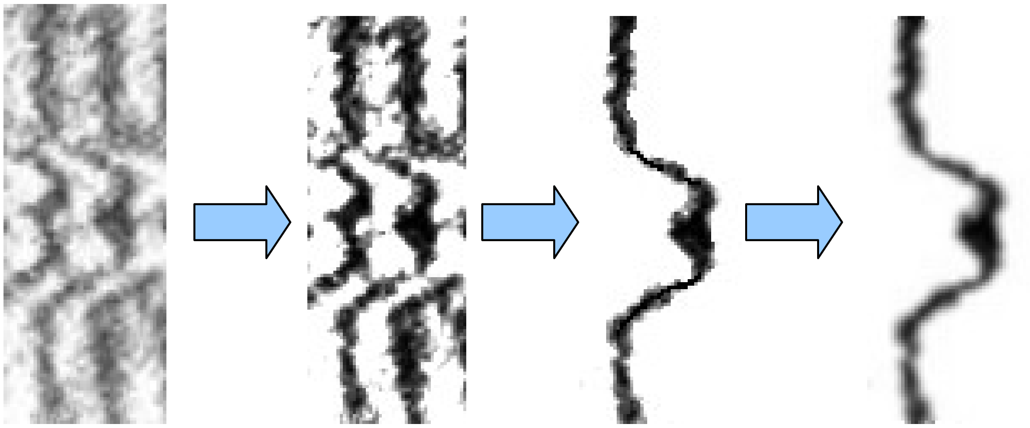

a) b) c) d)

Figure 3.3: a) Shows a cropped portion of an interferogram. Processing of the image includes b) adjusting the contrast level, c) selecting a single fringe, and d) smoothing the intensity of the fringe.

numerical noise at a level as high as 30% (especially at the center). In order to minimize the numerical noise the data was smoothed before and after the Abel inversion and the total error was decreased to 15%.

Chapter 4

Energy Deposition Results

Quantifications of the amount of energy deposited into a plasma are very important in that the information can be used to calculate the temperature of the plasma. For this experiment, it is important to note, when analyzing the resulting channels, both the input energy entering the gas cell as well as its absorption rate in order to best understand how the channel is effected by different parameters.

4.1 Energy Losses in Gas Cell

The setup used in this experiment is unique in that the geometry is a cross between the frequently-used capillary channel setup (utilizing the capillary material via surface ablation) and the traditional large-volume backfilled chamber. While the volume of the gas cell itself is large enough to ignore surface effects of the plasma channel development, the small pinholes through which the ionizing pulse must pass act similarly to the entrance of the microcapillary. Also, as there is a pressure gradient between the inside of the gas cell and the surrounding vacuum, a small amount of gas flows out of the pinholes, similar to the case of the microcapillary. In Chapter 2.2, the issue of the laser-matter interaction between the ionizing beam and the copper pinholes was introduced. In order to investigate the plasma produced at the pinholes as well as quantify the effect of the pinholes on the amount of energy available for ionization of the gas in the gas cell, energy measurements were made before and after the gas cell under several different conditions.

First, the energy losses due to the interaction of the ionizing beam with the copper pinhole without the presence of any gas was measured. The rear pinhole was removed and the transmitted laser energy as a function of incident energy was measured (see Fig. 4.1). At low incident beam energies, almost all of the incident energy passes through the gas cell practically without the laser interacting with the front pinhole. At higher energies, though, the intensity of the pulse farther from its axis increases and produces plasma via laser-induced ablation of the copper pinhole (see Fig. 4.2). This process can occur on the order of tens of picoseconds resulting in the formation of a plasma which acts to effectively close the pinhole and disallow the entire laser pulse energy from entering the gas cell. The energy losses due to this process are significant and reach ~40% at incident energies of 0.5 J.

The incident and transmitted energies were then measured with both the front and the rear pinhole in place. At lower energies, only 10% of the incident energy is lost due to the rear pinhole while, at higher energies, almost 20% of the energy is lost on the rear pinhole. As with the case of the front pinhole, the decrease in transmitted energy is further evidence for additional plasma creation due to the ablation of the rear pinhole. It is this plasma formed inside the gas cell which effects the uniformity at the end of the resulting plasma channel. At 100 ps, a very dense region with density > 3.9×10^{21} cm^{-3} (too dense to be imaged by the 532 nm interferometer beam – see Section 3.2) has

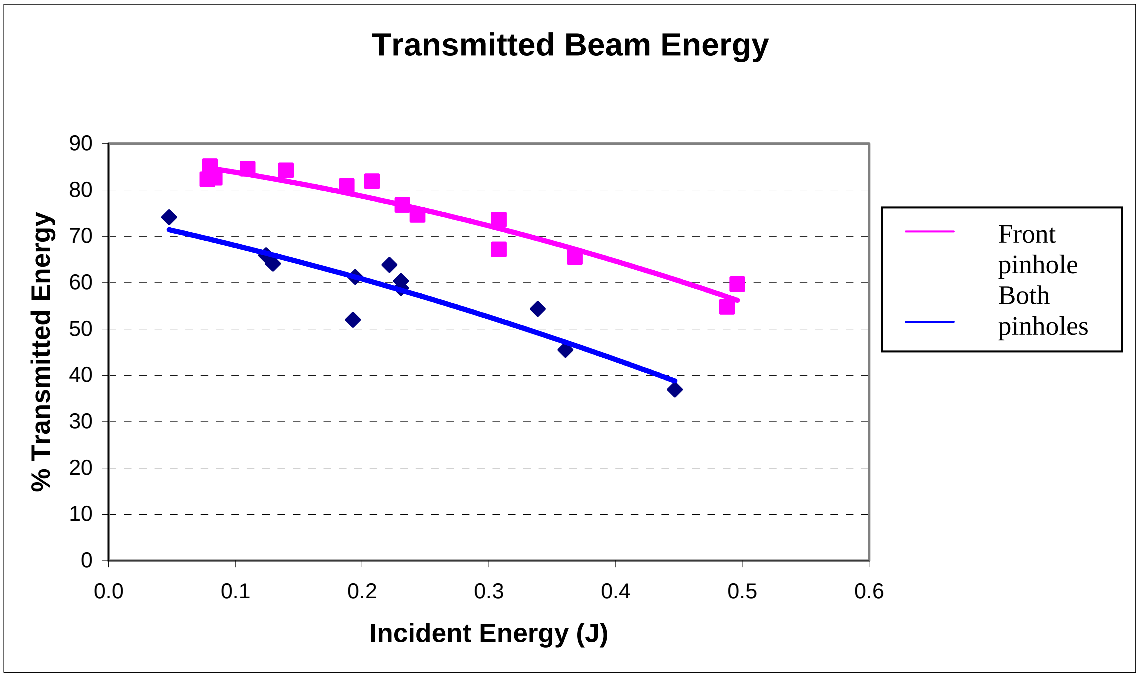

Figure 4.1: Transmitted laser energy across empty gas cell.

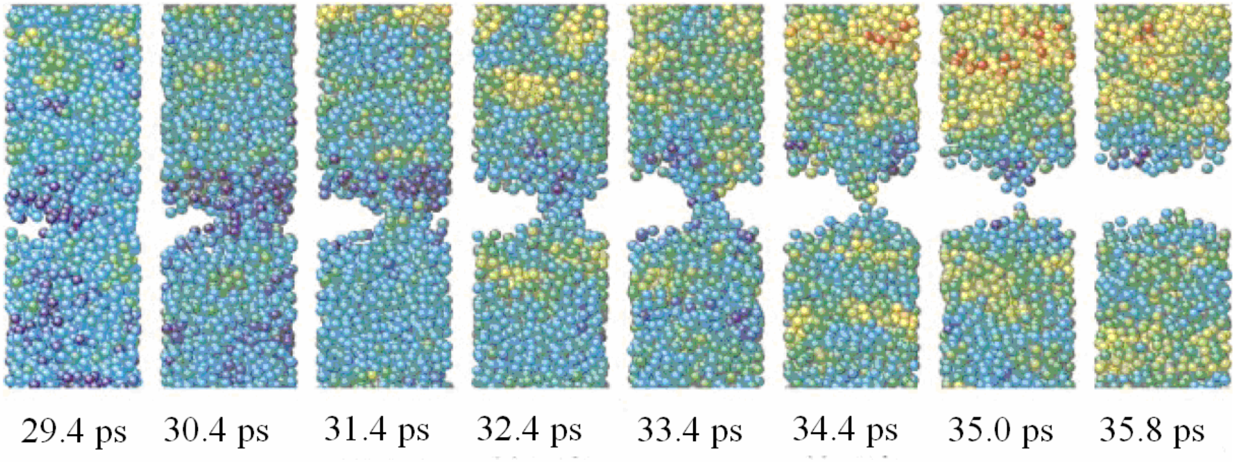

Figure 4.2: Atomist view of ablation of copper from a picosecond laser pulse [24].

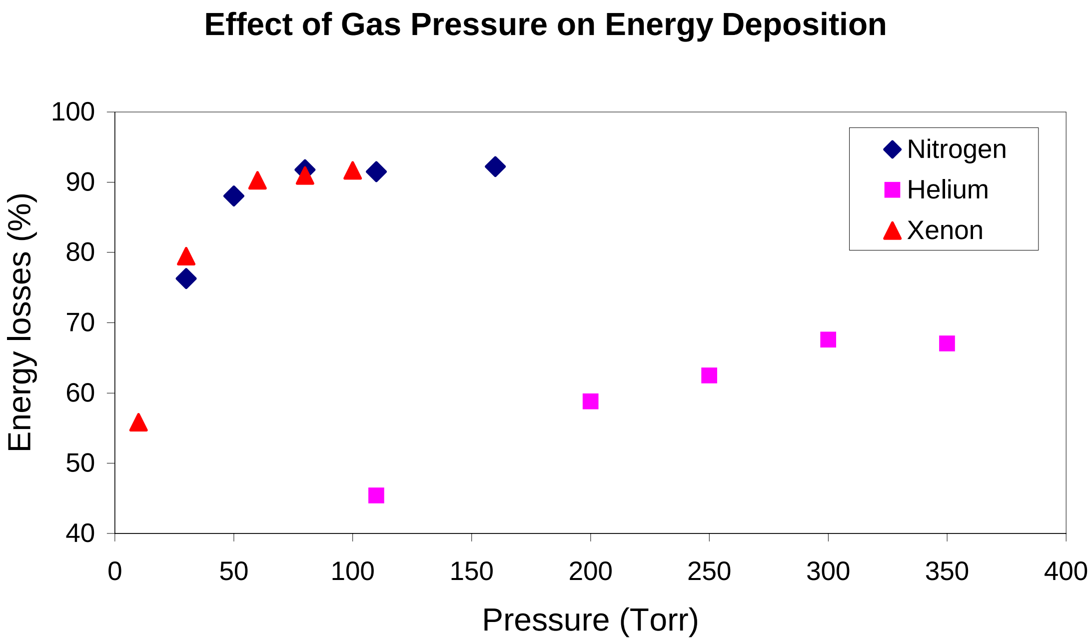

Figure 4.3: Effect of pressure on % energy losses.

already been formed (see Fig. 4.5). This plasma continues by expanding radially outward while its density decreases. By 600 ps, the outermost region of the pinhole plasma has decreased in density enough to produce distinct phase shifts in the interferogram. At this and later times, the radial density profile is shown in Figure 4.6 as it continues to expand radially and decrease in magnitude. Thus, with an understanding of the time scales and dynamical processes involved in the plasma formation at the pinhole, the channel generation can be better understood.

Once the effects of the pinholes alone were quantified, the incident and transmitted energies were measured as the laser passed through N_2, He, and Xe in the gas cell at different pressures. Figure 4.3 shows that the percentage of energy deposited in N_2, He, and Xe increases almost linearly with increasing pressure and then levels off.

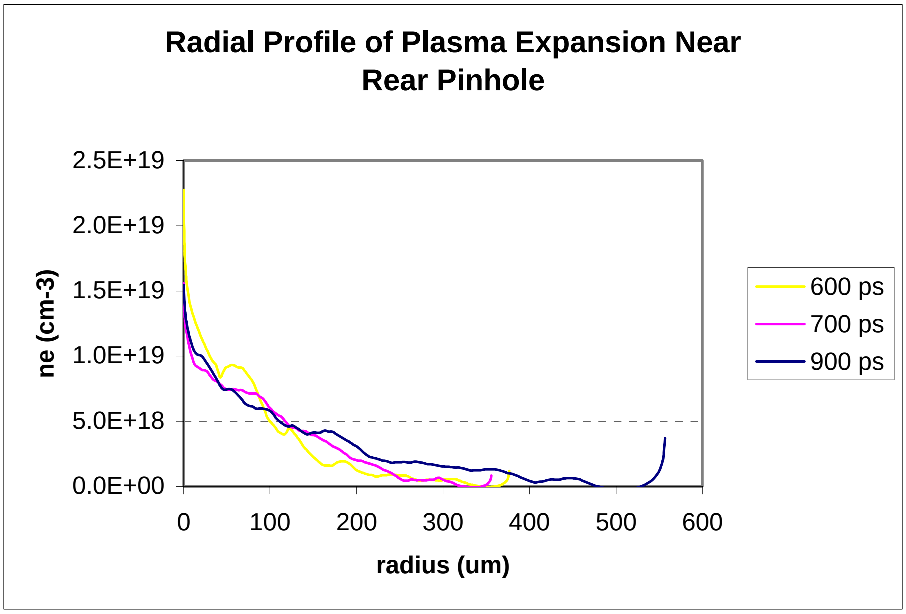

Figure 4.4: Temporal evolution of the radial electron density profile of the rear pinhole plasmas channel.

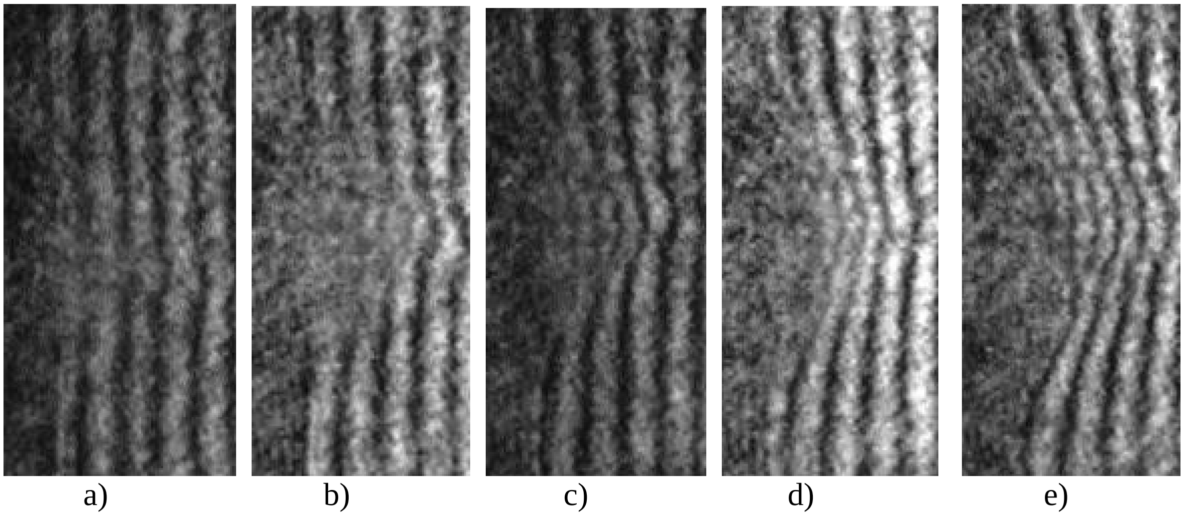

Figure 4.5: Rear pinhole plasma formation at a)100 ps b) 400 ps c) 600 d) 700 ps and e) 900 ps after the arrival of the ionizing beam.

The point at which these curves level off corresponds to the pressure at which increasing the incident beam energy no longer results in more energy being deposited into the gas. These pressures (~60 torr for Xe and N_2 and ~350 torr for He), as is discussed in Chapter 5, are the pressures used for most of the experiments done to increase the length of the plasma channels. The results shown in Figure 4.3 agree with those found by Milchberg *et al.* [28] for the energy loss of a laser beam in a Xe-N_2 gas mixture.

4.2 Measurement of Energy Deposition into Plasma

The deposition of energy into the plasma can be estimated from the thermal energy (E_{th}) of the expanding plasma. Clark *et al.* [26] illustrated the applicability of the model of expansion of a cylindrical shock wave for an estimation of E_{th} via the position of the shock wave front as

$$R(t) = \xi_0 (E_{th} / \rho_0)^{1/4} \tau^{1/4} \qquad 4.1$$

where ξ_0 ~1, ρ_0 is the gas density, and τ is the time of expansion. E_{th} is shown in Figure 4.6 for N_2 at 40 and 150 torr. For both pressures shown, the thermal energy is large close to the entrance of the gas cell due to the influence of the wall plasma. For lower pressures, the energy deposition is relatively uniform between 0.7 and 2.5 mm and is approximately 2-5 mJ. At higher pressures, almost no energy is deposited into the uniform region of the channel. An explanation for this may be that, due to the hot electrons produced by the ablative plasma, the energy absorption rate at the front pinhole may be large enough that only a small amount of energy is able to continue on, thus resulting in the nonuniform, short, low-density plasmas described in Chapter 5.

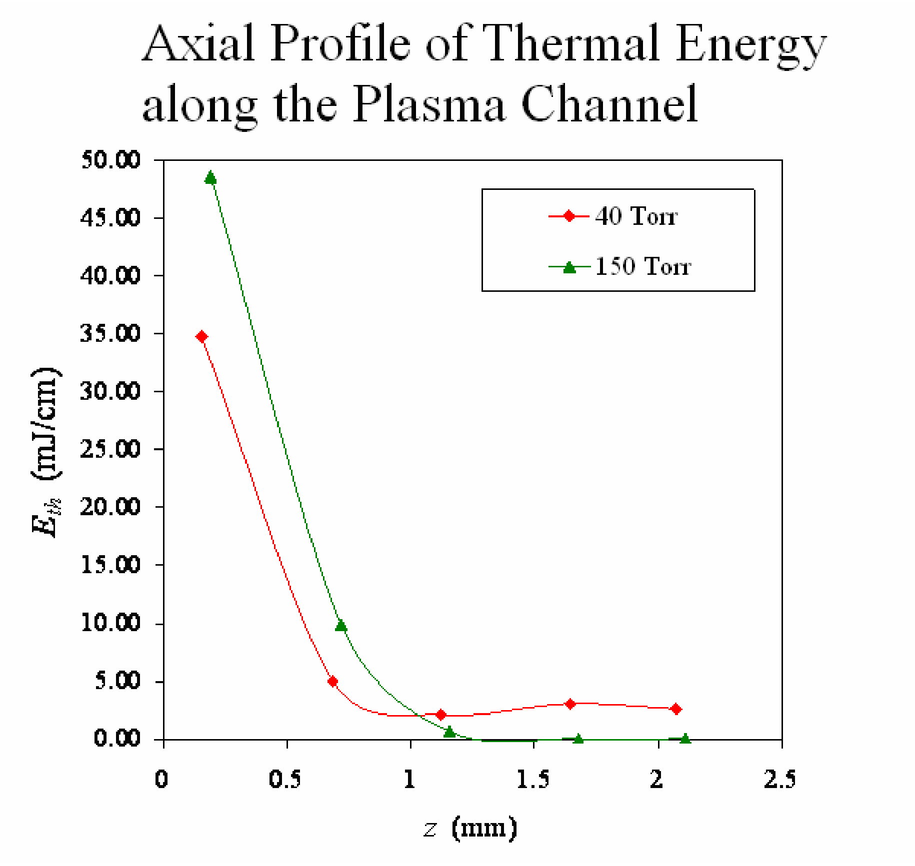

Figure 4.6: Thermal energy along the axis of the plasma channel.

Chapter 5

Plasma Channel Results

The primary objective of this experiment was to investigate the generation of a longer, more uniform plasma channel. To this end, the processes of plasma formation as well as how the resulting plasma channel is affected by a number of different parameters were investigated. The channel's dependence on various parameters was examined by using different gases in the cell, varying the gas pressure, inducing an initial electric breakdown with an applied DC voltage, and using an additional pulsed voltage source. Also, the temporal evolution of the channel was studied in order to give additional insight into both the properties of the channel and the dynamics involved. The experiment ultimately produces results which qualitatively agree with similar experiments done earlier, but also produces unique results due to the specific goals and setup.

5.1 Discussion of Ionization Mechanisms

Because plasma channels of varying specifications are integral parts of many different applications (particularly laser waveguiding), much modeling and experimentation has been done to investigate the processes of channel formation as well as its subsequent evolution. While it was beyond the scope of this project to model the plasma dynamics, I will rely on other works to discuss the physical processes involved in our experiment. In particular, the setup most similar to our experiment is that used by Milchberg [27] and Gaul [16], where a quiet gas in a backfilled chamber with large volume was used. Thus, while their analyses do not involve any of the pinhole effects occurring in our experiment, the main mechanisms involved in plasma formation and its evolution are similar. Finally, while there are many different regimes (corresponding to beam intensity, gas pressure, setup used, etc.) in which channels can form, I will only discuss those which closely relate to our experiment.

At lower pressures (on the order of <50 torr), ionization by the laser field is usually the main participant in the plasma formation. Within this pressure regime, the formation of a plasma channel generally occurs due to one of two processes depending on the ionizing laser's parameters: direct multiphoton ionization or tunneling ionization (ponderomotive acceleration and relativistic effects can be ignored for $I<10^{18}$ [29]). These two regimes are separated by the Keldysh tunneling parameter [30],

$$\gamma = (I_p / 2 \cdot \varepsilon_q)^{1/2}, \tag{5.1}$$

where ε_q is the electron quiver energy (or ponderomotive potential of the laser) and I_p is the ionization potential of the atom or ion. The ponderomotive potential is the average kinetic energy of an electron in the laser field and is defined as

$$\varepsilon_q = e^2 \varepsilon^2 / 4m\omega^2 = 9.33 \times 10^{-14} I\lambda^2 \tag{5.2}$$

where I is in W/cm^2 and λ is in μm.

For $\gamma>1$, multiphoton ionization (whereby the atom or ion simultaneously absorbs N photons) is the main ionization mechanism. In the alternate regime, when $\gamma<1$, the ionization is described as a tunneling process in which the high electric field produced by the laser lowers the Coulomb barrier enough to allow electrons to tunnel out of atomic or molecular bound states. For our experiment, the intensity of the 1064 nm laser is on the order of 10^{14} W/cm^2, and the ionization potential of N_2 is 15.6 eV. Thus, as the Keldysh parameter in this experiment is approximately 0.886 (close to the divide between multiphoton and tunneling ionization), it is most likely that, while both processes take part in the initial ionization of the gas, other processes are involved in producing the electron densities seen in the experiment. Once a small amount of initial electrons are produced, they are then heated by inverse bremsstrahlung before taking part in collisional ionization as they expand radially outward on a nanosecond scale.

At higher pressure regimes for the same laser intensity, avalanche ionization tends to contribute more to the plasma formation. The ion temperature tends to remain small due to weak electron-ion coupling, and the tunneling rate increases with laser field strength thereby allowing for increased ionization levels. Due to the space charge keeping the plasma electrically neutral, a well-defined boundary appears between the plasma and neutral, cold gas surrounding the plasma. This results in a large pressure gradient at the periphery which drives a shock wave pulling the electrons and ions outward resulting in an on-axis electron density minimum in the plasma [31]. The time scale for hydrodynamic evolution of the plasma channel can be described as

$$\tau = \omega_0 / c_s \qquad 5.3$$

where ω_0 is the radius of the shock wave and $c_s = (ZkT_e / m_i)^{1/2}$ is the speed of sound in the heated plasma. Thus, by measuring the expansion rate of the shock waves, the electron temperature of the plasma can be estimated [28].

5.2 Temporal Evolution of the Plasma Channel

The temporal evolution of the channel production is a very important part of the description of the plasma channel. An understanding of how the channel changes as a function of time gives insight into the dynamics and mechanisms involved in the channel's production and development. Soon after the laser passes through the gas, the channel begins to form along the beam axis. Initially, the highest density plasma forms at the focal spot of the laser (approximately in the middle of the cell – see Fig 5.2 a). The axial length of the channel then continues to increase until it reaches the back pinhole, where it interacts with the previously formed pinhole plasma (see Chapter 4). While the channel is axially expanding, it is also undergoing a radial expansion in which the thin, high density plasma originally oriented in a thin line along the center of the channel expands outward as increasing amounts of electrons are ionized and then accelerate as they are further heated. At about 700 ps, an on-axis electron density minimum begins to form and an annular plasma channel (as opposed to the previously cylindrical channel) is formed.

These results agree very well with those calculated by Milchberg and Durfee [31] and those measured by Clark and Milchberg [27]. Using the mechanisms described in Section 5.1, a calculation was performed to determine the ionization of Argon at 30 torr with an ionizing beam of 100 ps, 1064 nm and intensity $I \sim 10^{14}$ W/cm^2. The model predicted a radial density profile which evolves in accordance with the results of this experiment – originally, a narrow channel is formed which expands radially outward forming an on-axis minimum after approximately 500 ps. Given that the calculations agree with the results of this experiment, the physics can assumed to be similar thus confirming the dynamics described in Section 5.1. Furthermore, Clark and

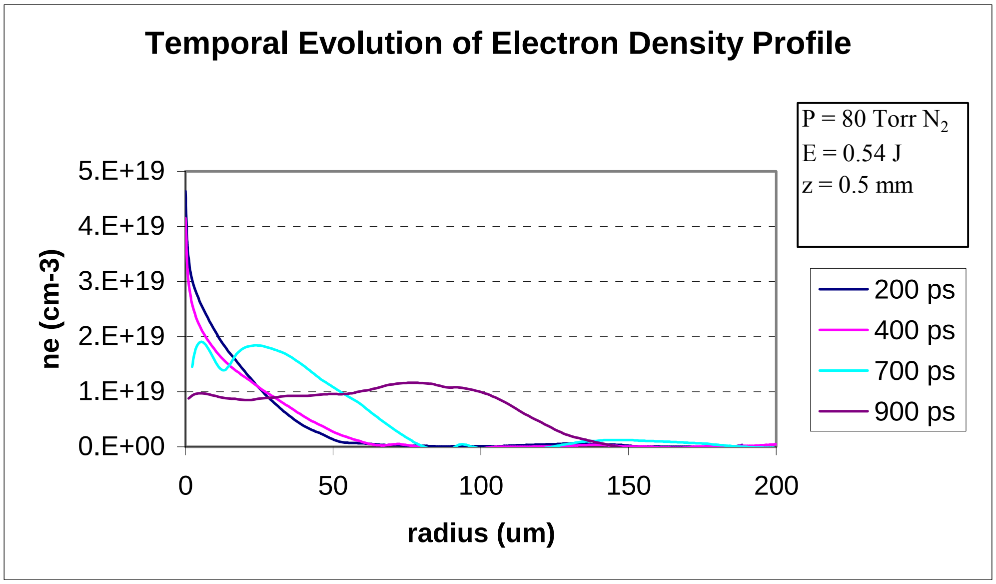

Figure 5.1: Temporal evolution of the plasma channel in N_2.

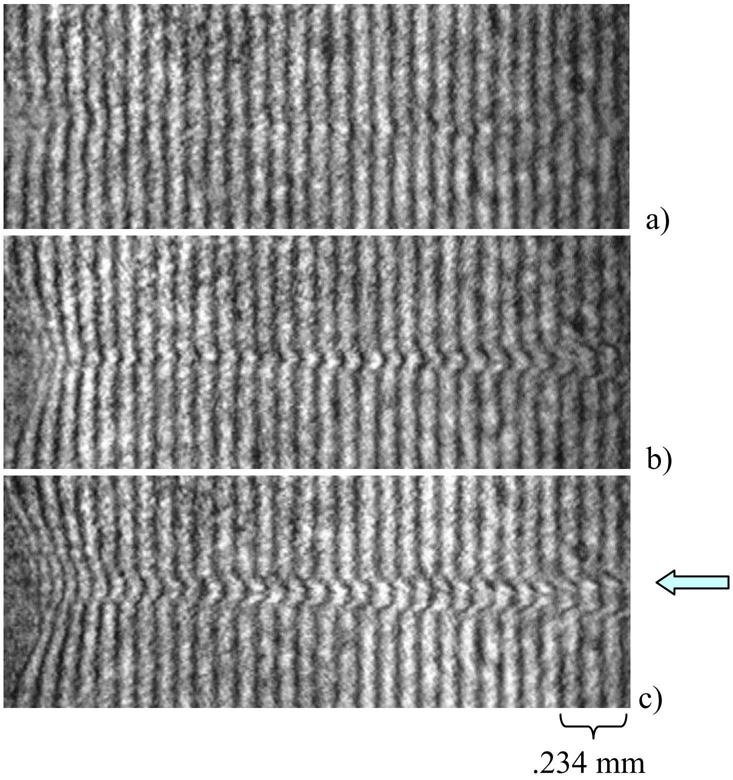

Figure 5.2: The plasma channel is shown here at a) 200 ps, b) 700 ps, and c) 900 ps after formation from N_2 with 0.54 J incident beam energy and at 80 torr.

Milchberg confirmed their calculations, thus further validating the results of our experiment. In their experiment, Kr at 150 torr was ionized in a backfilled container by a 100 ps 1064 nm laser beam with I~10^{14} W/cm^2. A 532 nm pulse was used as a diagnostic beam for interferometry, and the results, while differing slightly in electron density, agree well with the results of this experiment. Additional experiments and modeling were also done by Fan and Milchberg [32] and agree well with both the temporal evolution and electron densities produced in this experiment.

5.3 Effect of Gas Species on Plasma Channel

The plasma produced from a given ionizing beam varies depending on the gas being ionized. The factors which play a role in the resulting plasma channels include the masses of the atoms and ions involved and their ionization potentials. The interferograms and Abel inverted radial profiles show that N_2 has the highest electron density, followed by Xe and then He (see Fig. 5.3). Furthermore, after the same time (900 ps) the Xe channel is seen to have radially expanded to a radius of ~0.4mm while the He and N_2 channels are ~0.15 mm in diameter. All three channels, though, show that an on-axis minimum electron density occurs with a density maximum occurring at 0.03 - 0.1 mm from the axis.

The relative electron densities can be explained in terms of the relative ionization energies of the given gases. For Xe and N_2 the ionization energy required to remove the first electron is substantially smaller than that of He. Thus, it is to be expected that the electron densities of the plasma produced by ionizing N_2 and Xe should be similar to one another (with Xe being slightly lower due to its closed shell noble gas electron configuration), and should both be higher than that produced by He. This result agrees with that produced by Augst et al [15] where the tunneling ionization of noble gases ionized by high-intensity laser fields was investigated. In that experiment, a 1053 nm Nd:glass laser system was used to produce, after amplification, a 1 ps pulse which was varied in intensity from 10^{14} to 10^{16} W/cm^2. For the laser intensities used in our experiment, Augst demonstrates that 1 and 2 times ionized Xe and N_2 can be expected while He will be only singly ionized (if at all) due to tunneling ionization. Thus, the enhanced density of the He channel further indicates mechanisms beyond direct ionization by the ionizing beam (i.e. IB heating and collisional ionization) which contribute to the total electron density of the plasma.

5.4 Effect of Gas Pressure on Plasma Channel

In order to determine the optimal pressure for channel production for a given ionizing beam energy, a scan over different pressures was done for N_2, Xe, and He. Figure 5.5 illustrates the correlation between the pressure and the channel length for these gases. Plasma channels form in N_2 and Xe at low pressures (~30 torr) but no noticeable channels (i.e. a channel with density high enough to be resolved by the interferometer setup) formed in the He until above 100 torr. The necessity of higher pressure for channel formation with He can be explained by the fact that less electrons are produced in He than N_2 for the same beam energy. Thus, at the same pressure, the total density

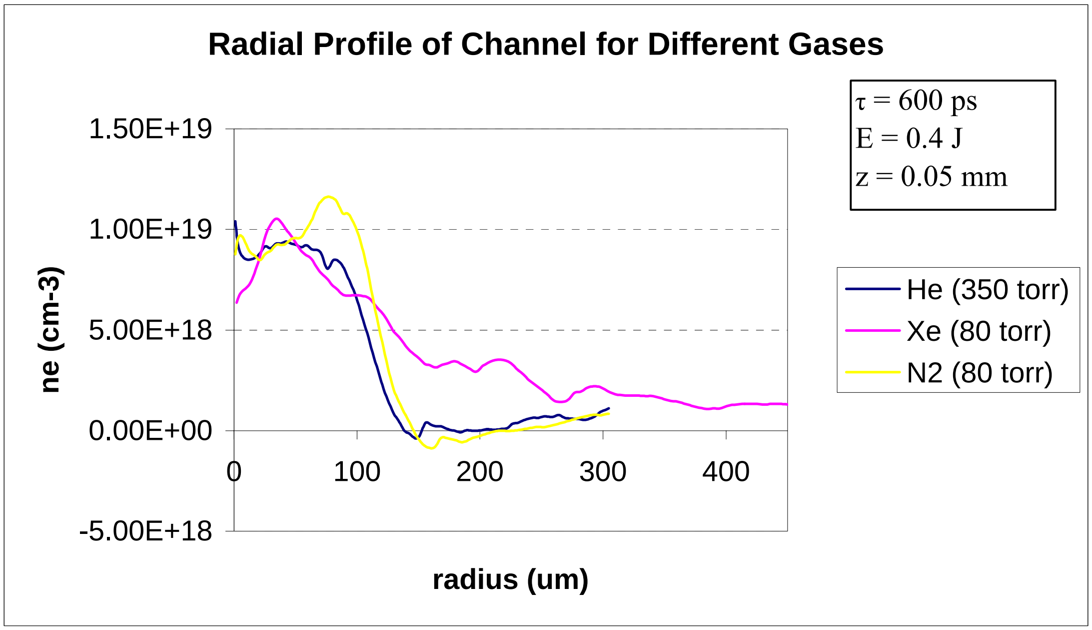

Figure 5.3: The radial density profile of N_2, He, and Xe at the beginning of the channel.

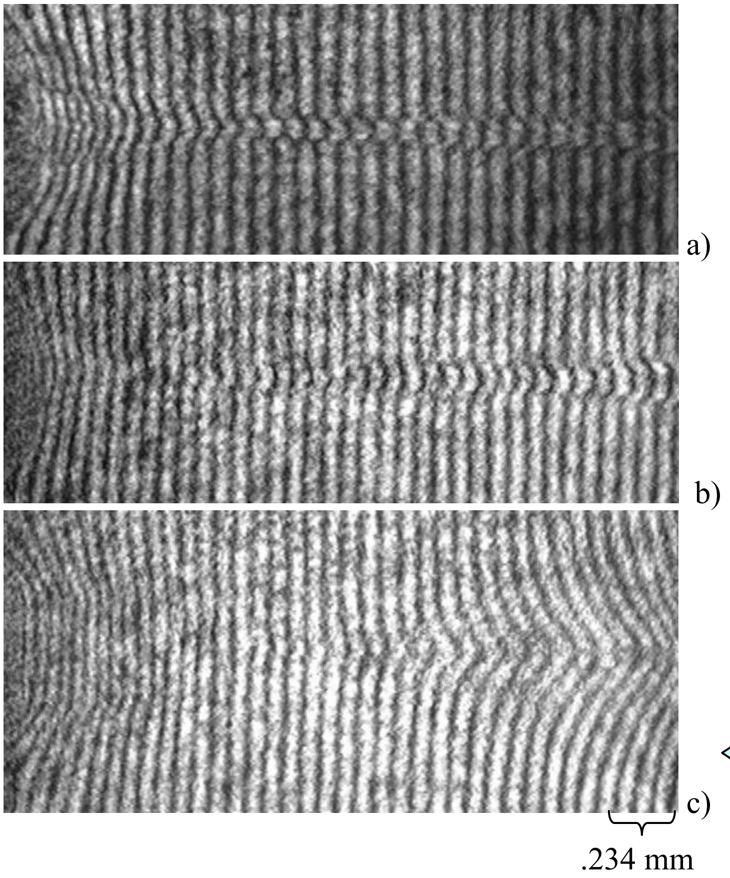

Figure 5.4: Interferograms of the plasma channels produced in a) N_2, b) He, and c) Xe.

beam

of electrons in He will be smaller than N_2. Still, this would only produce a density ratio on the order of 2-3 between N_2 and He whereas the density of He plasma at lower pressures must be at least an order of magnitude lower in order not to appear in the interferogram. This disparity may indicate the importance of collisional ionization as additional mechanisms which act to increase the electron density after the initial ionizing beam exits the cell.

The effect of pressure on the electron density both axially and radially is illustrated in Figures 5.7 and 5.8. In the axial direction, the plasma is observed to be somewhat uniform with a particular pressure producing the longest channel with a density in the acceptable region. Also, it can be seen that the radial profiles of the resulting channels at different pressures are similar in structure but also indicate an optimum pressure at which the density is maximal. Having noted that the maximum plasma length, as well as largest and most uniform plasma density, occurs between 60-70 torr for N_2, most of the succeeding experiments were done in this pressure range in order to optimize the other parameters.

An optimal pressure for producing the longest channel can be seen for Xe and N_2 at around 80 torr and 60 torr respectively (no such maximum is shown for He simply because the critical pressure was not reached). These pressures correspond to the pressures shown in Figure 4.5 (relating the energy deposition to the gas pressure) at which the energy deposition curve levels off. The reason that such a critical pressure exists is thus related to the ionizing beam's deposition of energy into the gas.

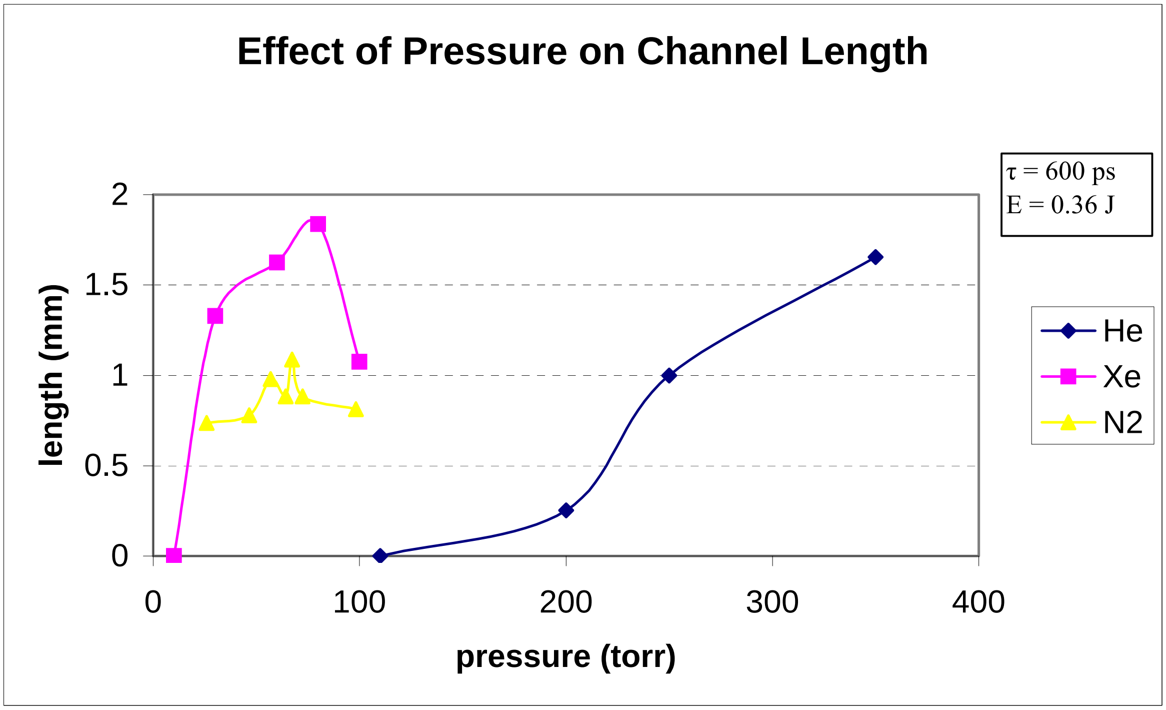

Figure 5.5: The effect of pressure on channel length for N_2, Xe, and He.

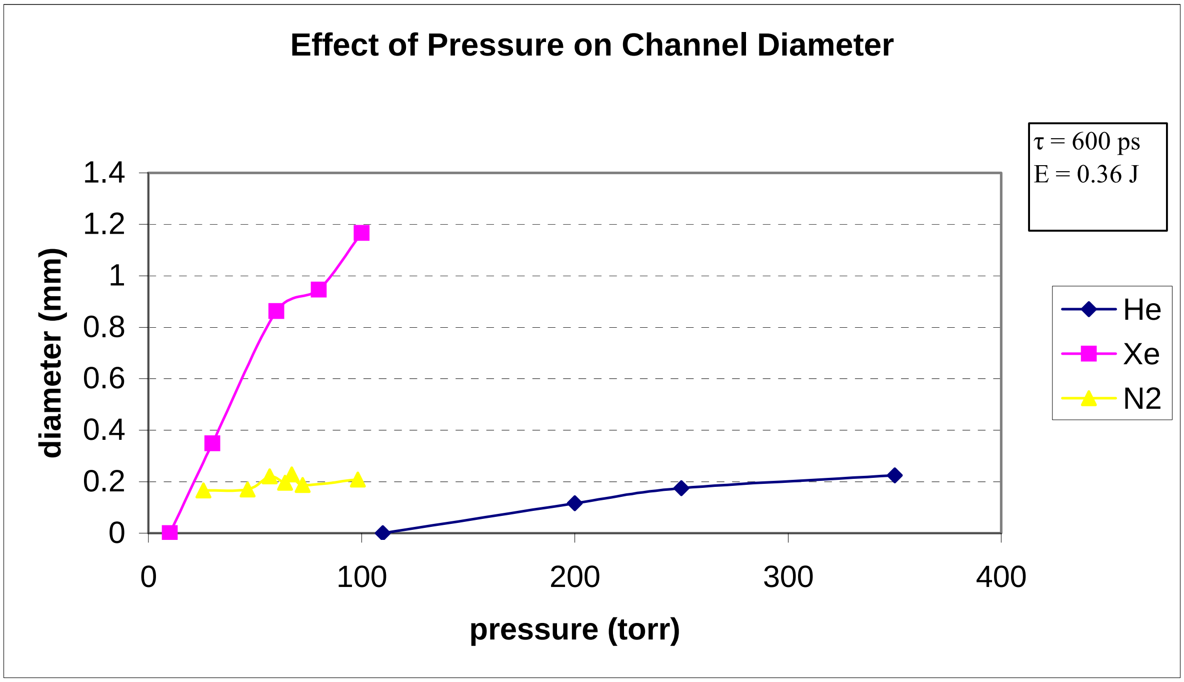

Figure 5.6: Effect of pressure on channel diameter for N_2, He, and Xe.

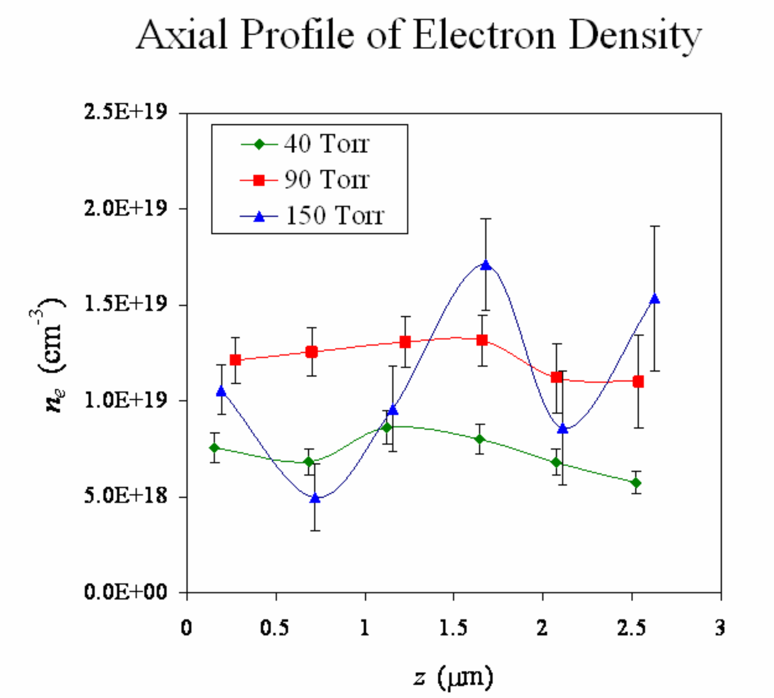

Figure 5.7: Relationship between electron density and the gas pressure along the length of the plasma channel.

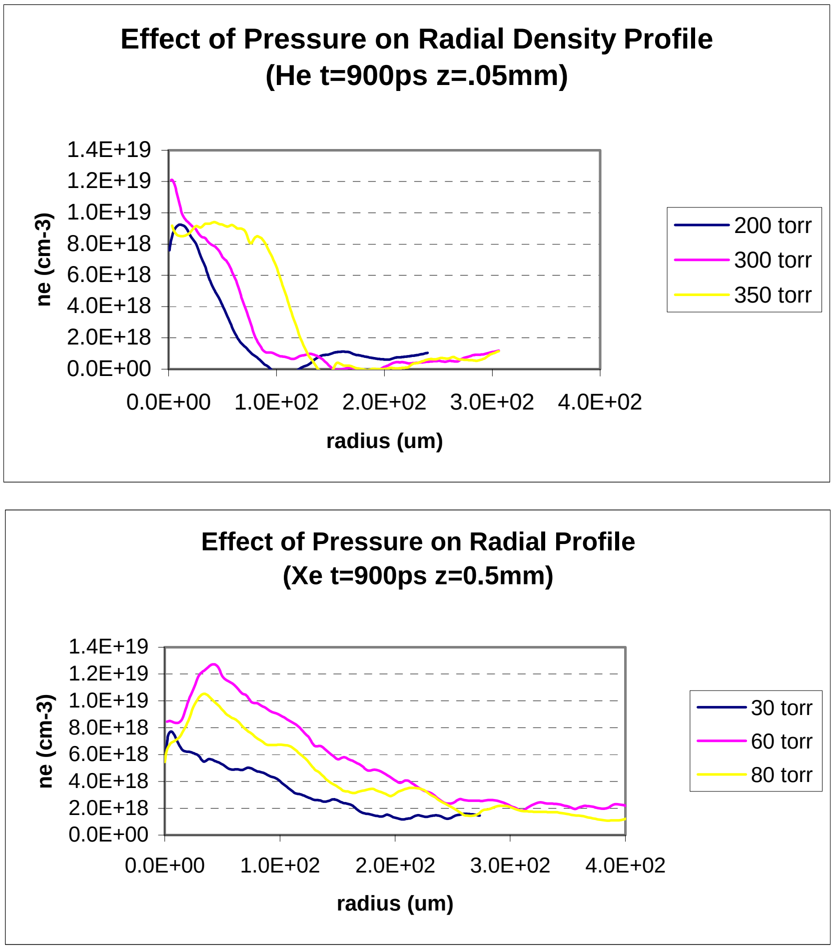

a)

b)

Figure 5.8: The effect of pressure is shown for a) He gas and b) Xe gas.

As the beam passes through the gas, the beam loses energy as the gas is ionized and electrons are accelerated. Below the critical pressure, the beam has enough energy to ionize atoms across the entire length of the gas cell – thus, increasing the pressure increases the number of electrons which can be liberated, thereby increasing the electron density across the entire channel. As the pressure increases, the beam ionizes more atoms per unit length and thus deposits its energy into the gas over a shorter length. After the critical pressure, the beam is unable to effectively penetrate the entire length of the gas while still ionizing the atoms, resulting in a shorter overall channel.

The pressure of the gas in the cell also affects the diameter of the channel produced. For all three gases, higher initial gas pressures resulted in channels with larger diameters (see Fig. 5.6). This result also agrees with the mechanism of hydrodynamic expansion described in Section 5.1 – with increasing pressure, the pressure gradient between neutral and plasma regions of the gas increases, thus increasing the rate of outward expansion. Recombination, regardless of the pressure, will not have a significant effect on the resulting densities because such effects do not begin to play a major role until at least several nanoseconds, whereas the plasma in this experiment is being investigated on the order of several hundred picoseconds.

5.5 Effect of Pulse Energy on Plasma Channel

The pulse energy of the ionizing beam, directly related to the beam intensity, plays a major role in determining the characteristics of the generated plasma channels. Figure 5.10 shows that increasing the beam energy produces a longer plasma channel up

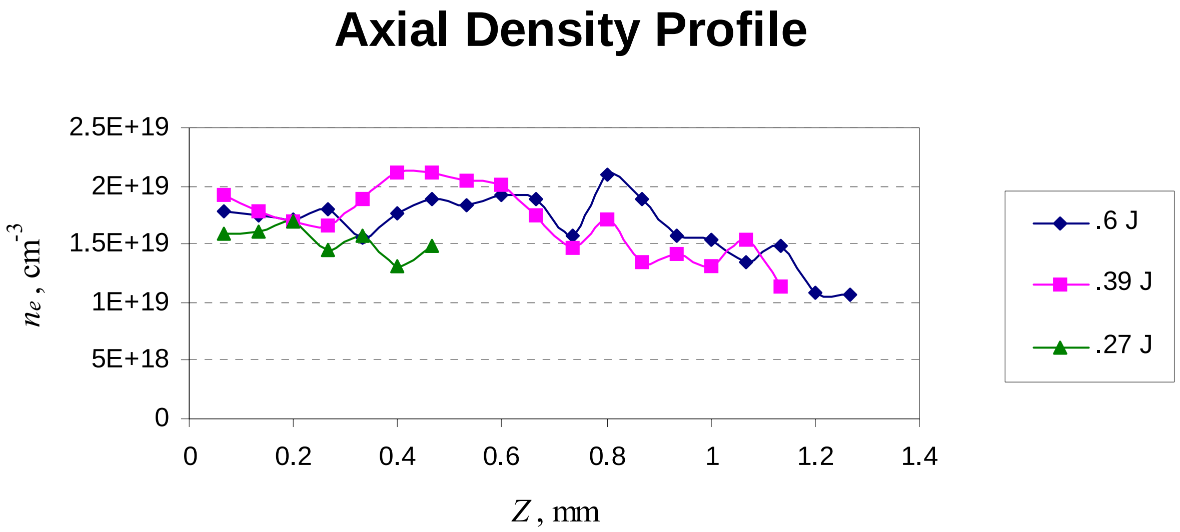

Figure 5.9: Relationship between the electron density and the pulse energy along the length of the plasma channel.

to a certain point. For N_2 and He, the maximum length occurred at approximately 0.4 and 0.5 J respectively. A larger laser energy could be expected to produce a longer plasma channel because it can penetrate further into the gas while still remaining with enough energy to continue the ionization process. At the same time, though, higher pulse energies produce larger degrees of ionization along the propagation path, causing larger amounts of ionization per unit length. Ultimately, this results in the beam's energy being fully absorbed at shorter lengths producing a shorter channel.

Larger incident beam energies also produce a channel with a larger diameter (see Fig. 5.11) for both gases. The energy of the incoming beam should affect the diameter of the plasma for two reasons. First, at larger energies, the laser intensity at larger radial distances is larger, thus potentially allowing for increased amounts of initial ionization further from the beam axis. Second, with a larger electric field present, the produced

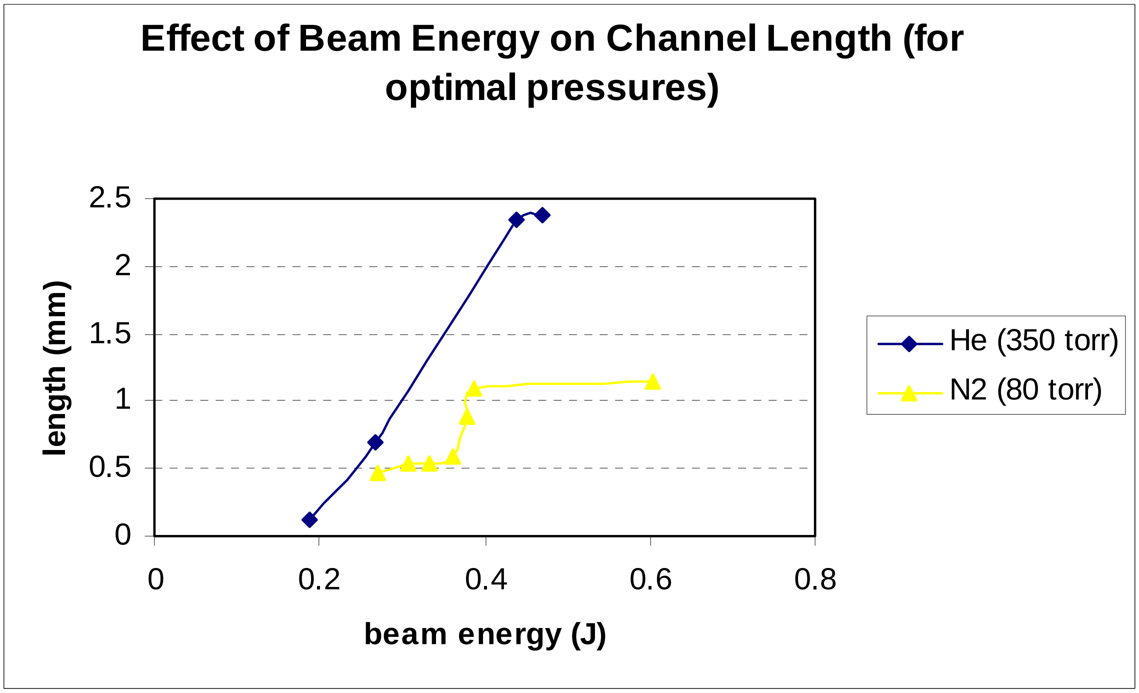

Figure 5.10: Effect of the pulse energy on the length of the plasma channel.

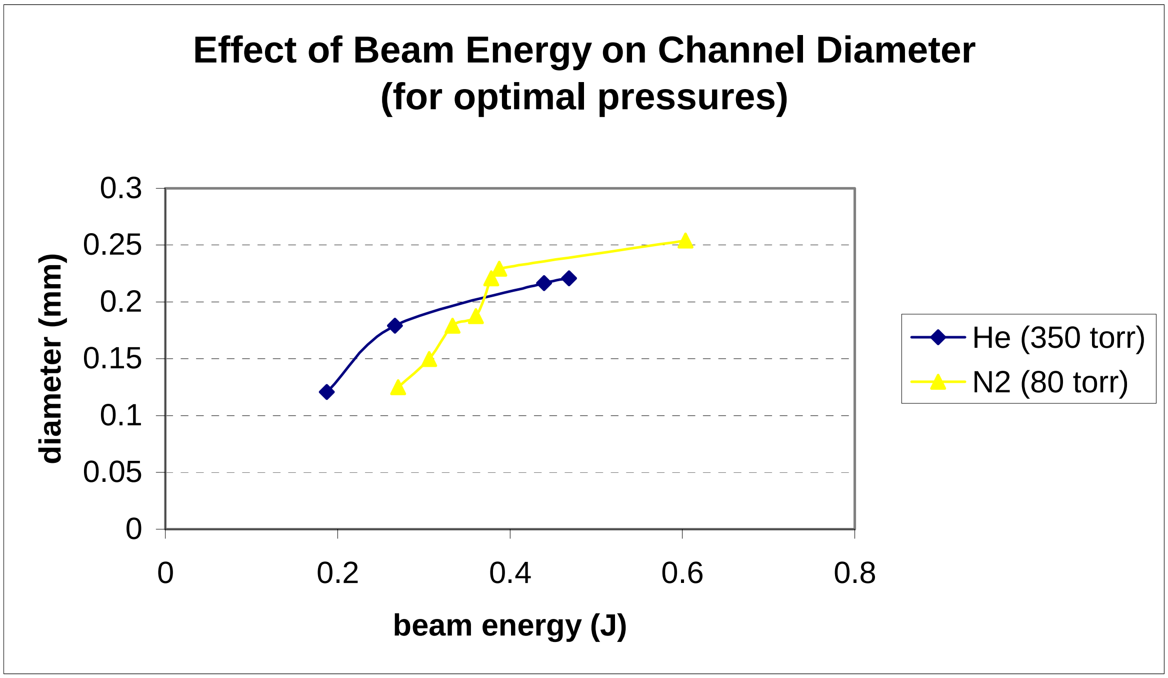

Figure 5.11: Effect of the pulse energy on the diameter.

electrons will be further accelerated and will thus cause the plasma to expand faster, resulting in a larger plasma diameter at a fixed time.

The electron density of the plasma along the axial direction for different beam energies is shown in Figure 5.9. The density can be seen to be approximately constant along the length of the channel regardless of incident beam energy (within the small energy and intensity range used in this experiment). The main effect on the channel of varying the incident beam energy was to produce plasma channels of varying lengths but with approximately equal densities. This, therefore, shows that increasing the beam energy effectively increases the beam's capacity to efficiently penetrate farther into the gas, but does not greatly affect the degree of ionization . Throughout the rest of the experiments, an incident beam energy of ~0.4 J was used to maximize both length and uniformity of the plasma without producing large amounts of pinhole plasma which reduce homogeneity.

5.6 Channel with Discharge

The motivation behind using a discharge is twofold – first, the discharge can act to pri-oinze the gas, allowing higher densities to be achieved with the same ionizing laser energy. Second, the discharge can be used for better guiding of the beam as it passes through the gas, resulting in a more linear channel that is more effective for waveguiding as well as mediating the interaction of the main, counterpropogating beams involved in the RBS scheme. Two different types of discharges were used in this experiment – a glow discharge and a pulsed discharge producing a spark.

5.6.1 DC Glow Discharge

A glow discharge, so called for the luminous plasma produced, is formed by applying a voltage across a given length of gas. The voltage distribution in the gas (see Fig. 5.12) consists of three main regions – high electric field regions at the anode and cathode known as the anode and cathode sheath, and the plasma region where the electric field is constant and small (due to the quasineutrality of the plasma). The glow discharge thus results from electrons being accelerated by the established field which closes the electrical gap between the electrodes and allows current to flow. Thus, while steady state conditions are met in the plasma, the plasma is not in thermal equilibrium, resulting in the production of hot electrons while the ions and atoms remain cold.

In our experiment, the gas cell setup was modified by applying a voltage between the entrance and exit pinhole material (see Chapter 2.3). With this 2 kV DC source drawing 1.6 mA, it can be seen that (see Fig 5.13) that a glow discharge is produced. According to Paschen's Law, the minimum voltage required for breakdown is

$$V_{\min} = B \cdot p \cdot d / (C + \ln(p \cdot d)) \qquad 5.4$$

where C =ln(A / ln (1 + 1 /γ)) and A, B, and γ are empirical and depend on the gas species. For Nitrogen, the minimum voltage required to strike a discharge for p·d=0.7 torr cm is ~250 V. Thus, with 2 kV applied at a p·d value of 18 torr cm (for p = 60 torr, d = 0.3cm), the regime established in the experiment can be seen to fall to the far right

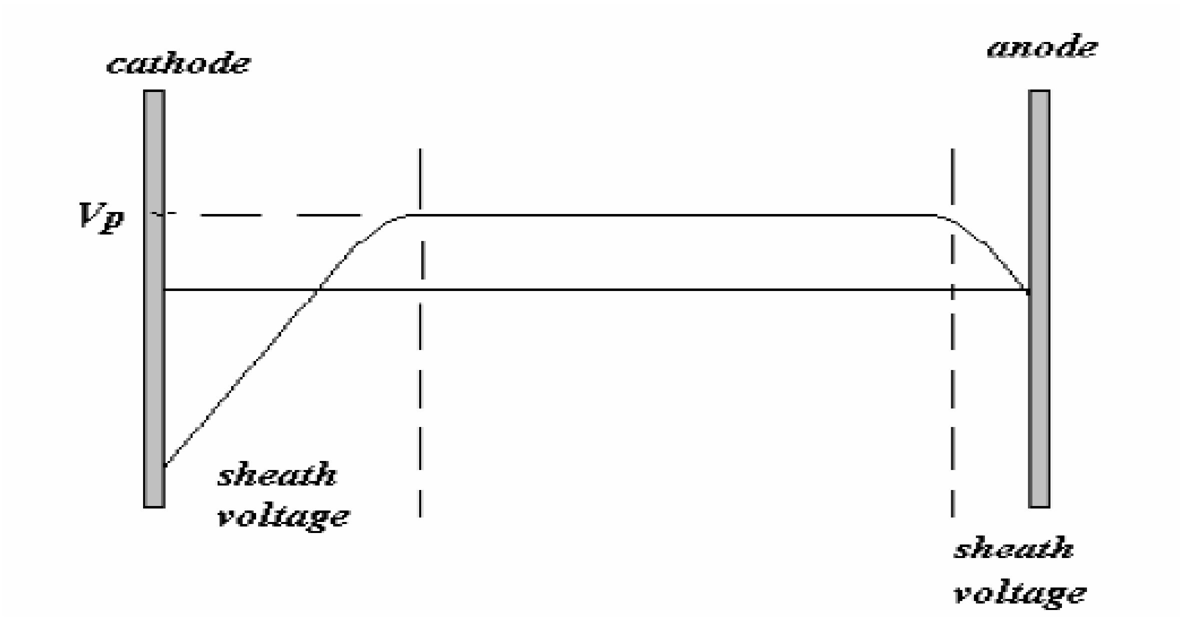

Figure 5.12: Voltage distribution in a glow discharge [33].

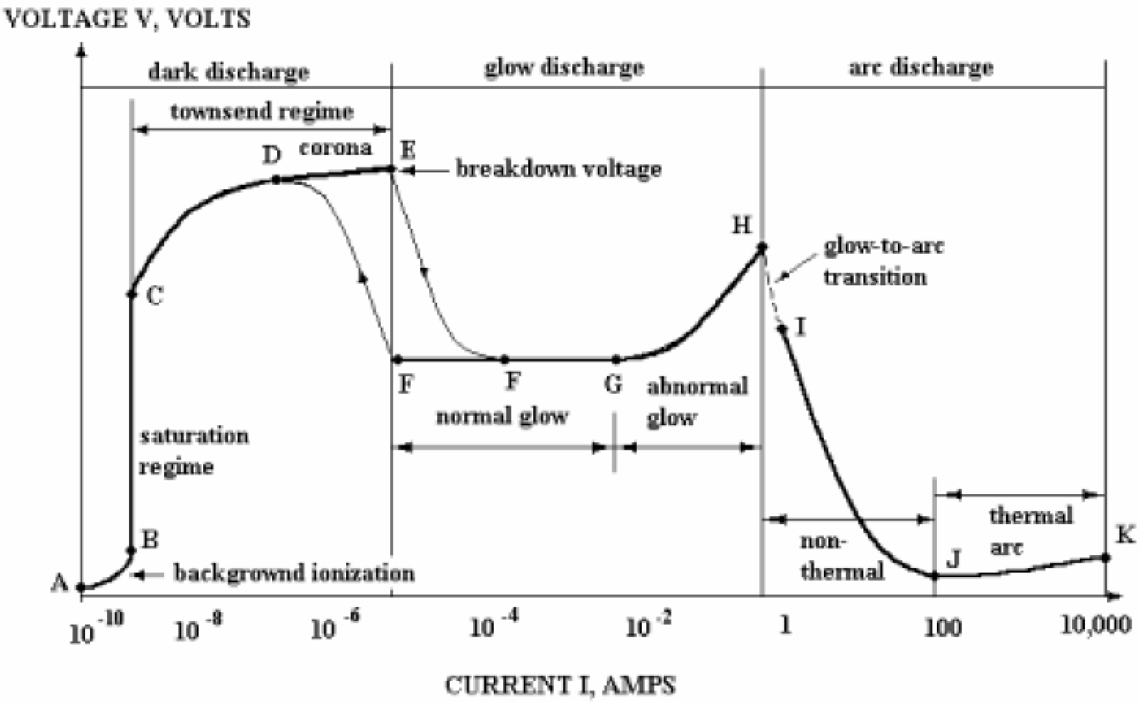

Figure 5.13 Diagram illustrating different discharge regimes [33]

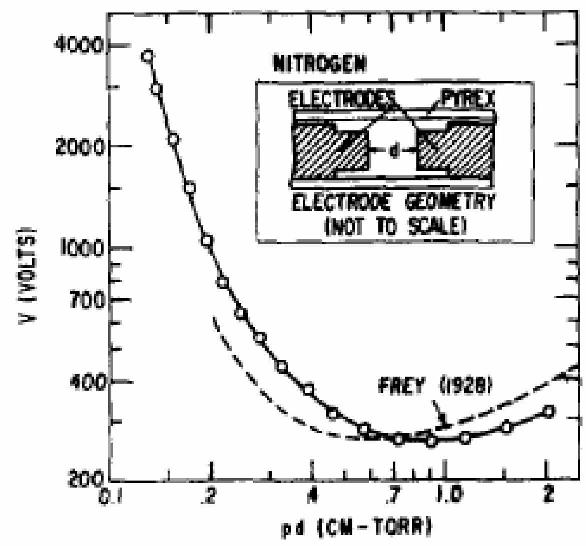

Fig 5.14: Paschen curve for nitrogen gas [34].

of the minimum breakdown on the Paschen curve (see Fig 5.14). This made it difficult to stably strike the discharge solely between the two pinholes because of the large relative pressure difference between the inside and outside of the gas cell. The glow discharge would sometimes be created between the two pinholes inside the gas cell (where the pressure was higher but the distance very small), and other times it would be struck outside the gas cell (where the distance was larger but the pressure was very small). Ultimately, a stable discharge inside the gas cell was produced at pressures of <30 torr, while the glow discharge produced at higher pressures was highly unstable and jumped from between the pinholes to between the front pinhole and the body of the gas cell (see Fig 2.8).

The electron density of the discharge is negligible on its own account, but was meant to produce seed electrons to enhance ionization from the laser. While both

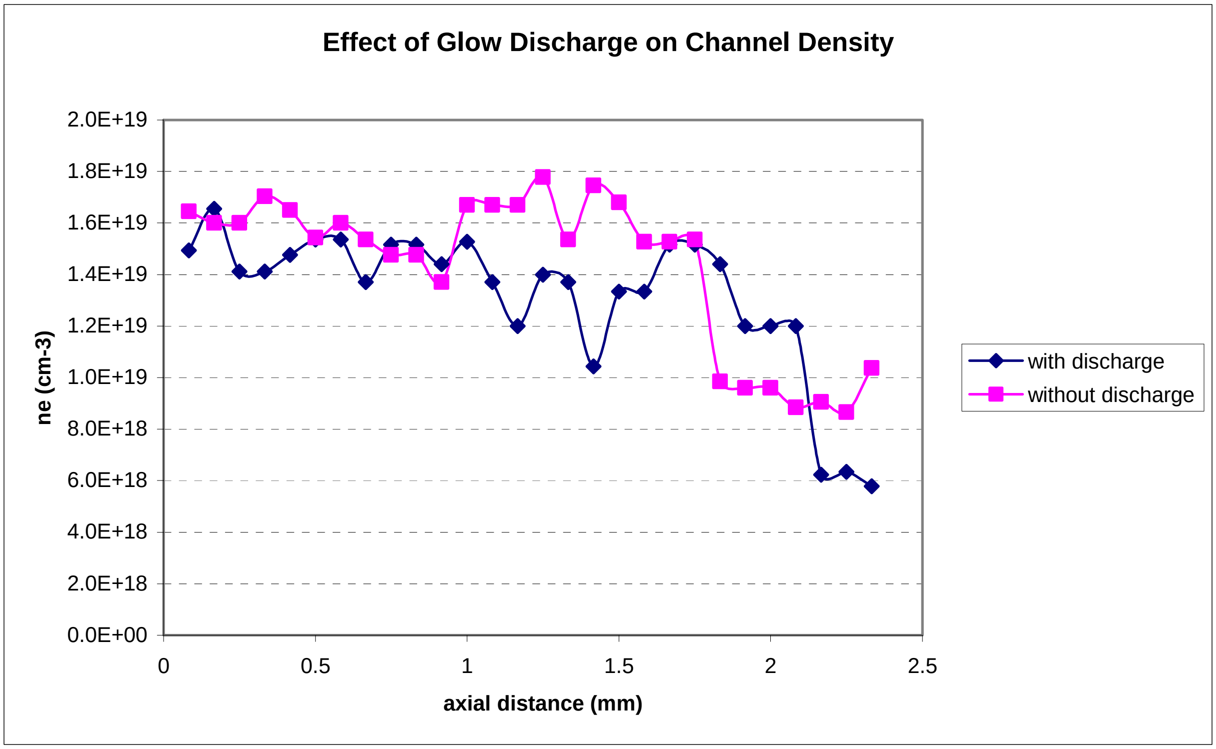

Figure 5.15: Axial Density profile of the channel produced with the glow discharge and without the glow discharge.

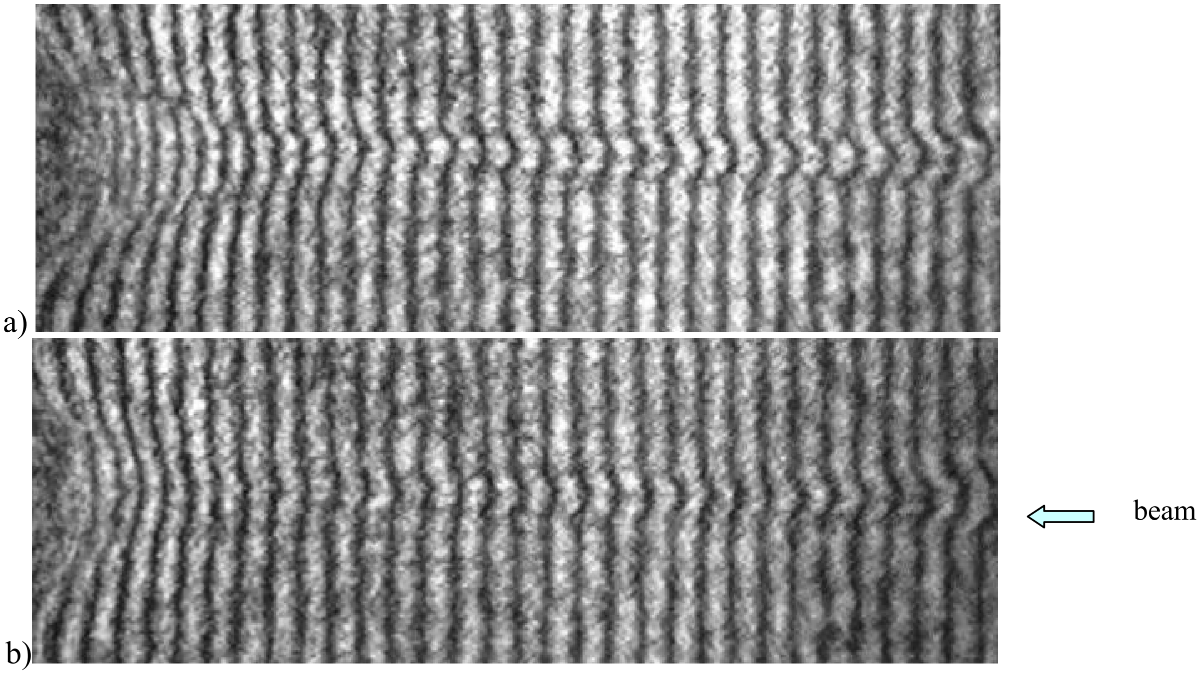

Figure 5.16: Interferograms of the produced plasma channel at 0.3 J, 40 torr and a time delay of approximately 900 ps. (a) Channel without glow discharge. (b) Channel with glow discharge.

channels (with and without the glow discharge) have approximately the same shape, length, and overall density (see Fig. 5.16), the size of the plasma from ablation of the rear pinhole is reduced when the glow discharge is present. This allows the uniform region of the plasma channel to extend farther than in the case without discharge (see Fig. 5.15). Thus, while the glow discharge does not enhance the density of the resulting channel, it does increase the uniformity at the end of the channel and allow for easier access to the channel for the pump and seed pulses as part of the RBS scheme.

5.6.2 DC Glow and Electric Pulse Discharge

In order to further develop the technique of using an electrical discharge in conjunction with the ionizing laser pulse, an additional 20 kV pulsed electrical source producing ~100 mA of current was connected to the pinholes (see Chapter 2.3). With this amount of current, a spark discharge is produced (see Fig. 5.13), although it was found that the initiation of the DC glow prior to the pulsed current was a necessary condition for production of the spark. The idea behind using a pulsed source is that, by timing the pulse just right, the applied voltage will preionize atoms allowing the ionizing beam to produce a more uniform channel of increased length before being absorbed.

For the setup using the spark gap (see Figure 2.4 a), a 200 ns, 300 A current pulse reached the gas cell at varying times prior to the arrival of the ionizing beam. The results are shown in Figure 5.17 a). Approximately 6000 W are injected into the gas resulting in the production of a very dense plasma spark in the gas cell. While the density of the plasma is not enough to show up in the interferogram without the presence of the ionizing laser, it is enough to noticeably effect the resulting channel. Just as in the case discussed in Section 4.2, the formation of a dense plasma bubble by the spark effectively disallows the laser pulse from penetrating into the gas. This can be seen from noting that neither the plasma channel nor a substantial ablative plasma is formed. In the second electrical setup (see Figure 2.4 b), a 200 ns 100 A pulse was used. This time, with less current, the density of the spark formed by the discharge is small enough to allow the laser pulse to penetrate the high density region, resulting in a nonlinear, nonuniform channel (see Fig 5.17 b). Also, the resulting channel differs greatly from shot to shot with all of the physical parameters held constant. This is most likely due to instabilities and variations in the location and density of the spark produced. Despite this, the interferograms shown in Figure 5.17 b) show that this setup may work better than the prior. The reason for this is that, with a smaller current, the reduced density spark does not interfere as much with the propagation of the ionizing beam. Thus, it could potentially be used to increase the electron density in the channel without the negative consequence of hampering the desired ionization resulting from the laser pulse.

The methodology is similar to that used by Gaul *et al.* [16], where a 100 ps, 0.3 J Nd:YAG laser was used along with a pulsed voltage source to generate a plasma channel. In that experiment, a preplasma (with electron density on the order of 10^{16} cm^{-3}) was produced by using two knife-edge electrodes immersed in the plasma with a 30 kV potential across them. The result of the work of Gaul *et al.* was not to increase the length of the 2 mm plasma by Milchberg *et al.* [35] but, rather, to more completely and uniformly ionize the gas (especially at its entrance and exit). Thus, the positive results obtained by Gaul *et al.* demonstrate the potential effectiveness of combining AC voltages and laser induced plasma formation in order to create greater plasma uniformity.

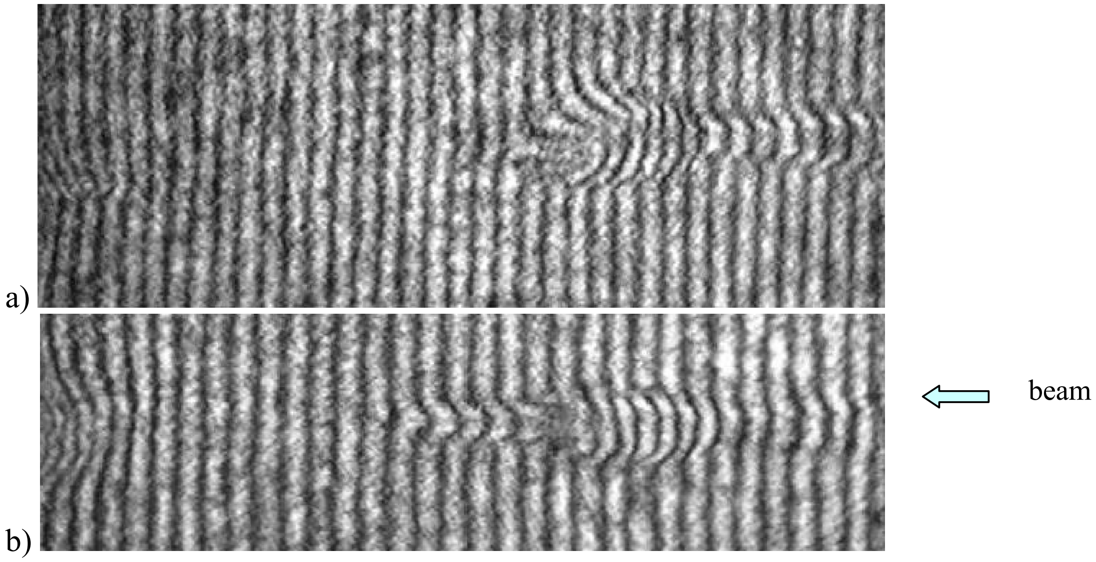

Figure 5.17: Interferograms of the plasma channel made with a) the first and b) the second electrical setup.

Additionally, while several groups (Hooker *et al.* [36], Zigler *et al.* [37]) have managed to make use of pulsed discharges to increase the length of the plasma channel in capillary tubes, no groups to date have reported any plasma channel lengthening due to electrical discharges in an open-volume or backfilled chamber.

Chapter 6

Conclusion

6.1 Summary

In this report, I have outlined the motivations for the further development of longer, more uniform plasma channels as well as presented the results of this experiment. At the beginning of the experiment, the best result that could be achieved was a very nonuniform, 1.3 mm plasma channel. After modifying and improving the preexisting setup, a quite uniform plasma channel (nonuniformity ±3.5 %) of approximately 2.5 mm in length with an electron density of 1.2×10^{19} cm^{-3} was produced in N_2 (see Fig. 6.1). The radial density distribution along the axial length of the channel has an on-axis minima in the region of uniform plasma density but is uniform, and less dense in the region affected by the ablative plasma (see Fig. 6.2).

The channel's variation with respect to a number of different parameters was also investigated. The gas species determines the ionization energy of the atom or molecule and thus effects the overall electron density produced. Ultimately, it was found that higher laser energies at a pressure of approximately ~70 torr (for N_2) produce longer and more uniform channels. Additionally, the use of a DC glow discharge in conjunction with the main ionizing beam can reduce the formation of the pinhole plasma and improve the overall density uniformity of the plasma. Also, while not successfully employed in this experiment, a pulsed electrical discharge appears to have potentially positive effects if the current is not too large and it is timed correctly with respect to the ionizing beam.

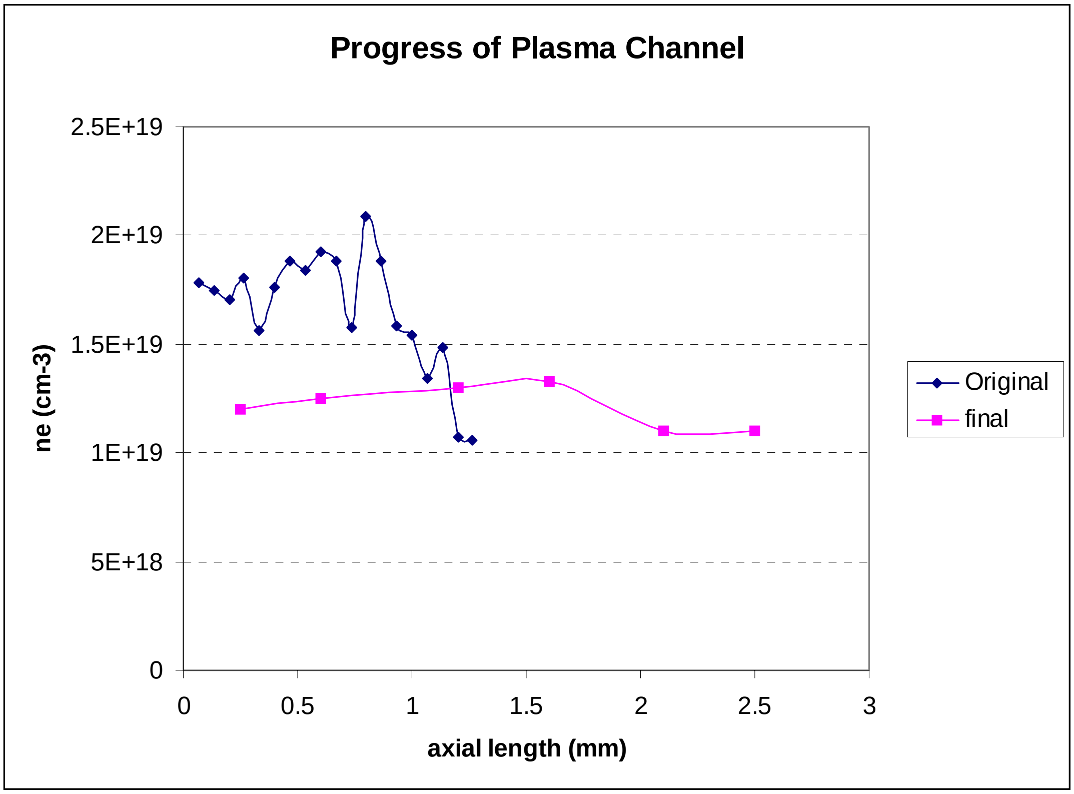

Figure 6.1: Progress toward creating a longer, more uniform plasma channel.

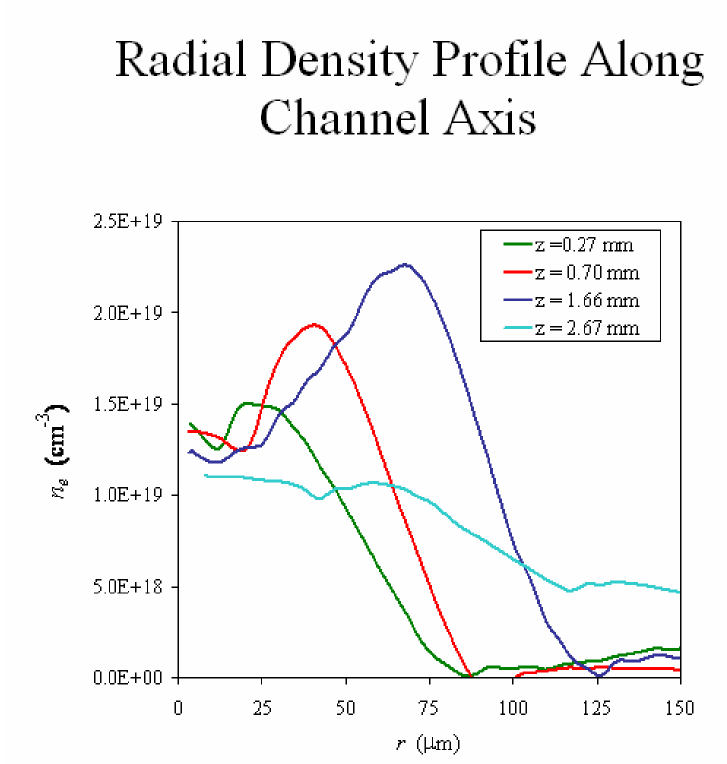

Figure 6.2: Radial Profile of the channel density for N_2 at 90 torr, t = 800 ps.

In order to appreciate the progress made, the 2.5 mm plasma channel produced must be compared to other channels produced to date. As was mentioned in Chapter 1, the problem of producing longer, more uniform channels is mainly a technical challenge. Multi-terawatt systems have reported producing channels on the order of 4 mm [38], very uniform plasma channels have been produced with the use of an axicon [27], and channels exceeding 15 mm in length (but with lower densities) have been produced through the use of gas clusters in microcapillary tubes [23]. Keeping in mind both logistics as well as the intended application of the plasma channel to RBS amplification, the downsides to the previous schemes become clear – multi-terawatt lasers are extremely expensive, using an axicon in the beam line of the ionizing beam is difficult to implement because both the seed and pump pulse must pass through the gas cell in the same direction as the ionizing beam, and the capillary plasmas generally have reduced densities and geometries better suited to waveguiding than to mediating pump-seed energy transfer. For our experiment, the design of the gas cell and optical setup and the resulting plasma channel are tailored for the resonant RBS amplification scheme. Thus, while a channel greatly exceeding the 2 mm plasmas produced by gas jets was not yet achieved, many steps have been taken toward characterizing and understanding the dynamics of the plasma channel as well as increasing the length and uniformity of the resulting channel.

6.2 Future Work

As is the case with any experiment which is constrained by a deadline, there are many more things which can be done. First, I would redesign and rebuild several components of the gas cell setup. In particular, many of the components inside the vacuum chamber are metal since the gas cell was not originally designed to be used with electrical sources. Thus, I would cut down on the amount of conducting elements within the vacuum chamber as well as electrically insulate the gas cell so as to allow for a more stable glow discharge. Also, I would increase the space between the pinholes so that the length of the plasma channel is not constrained by the distance between the pinholes.

Next, I would continue where I left off investigating the effect of varying the delay time between the electrical discharge setup and the arrival of the ionizing beam. Hopefully, an optimal timing for this setup can be found such that the discharge decreases the load on the laser beam to ionize all of the gas by itself so that it may penetrate further into the gas thus producing a longer channel. If I still did not find any such timing, I would then continue redesigning the electrical scheme to vary the current running to the gas cell so that the spark would not interfere with the ionizing beam but would, rather, simply enhance the final channel.

.

References

[1] Chirped-Pulse Amplifier Laser Systems. http://www- phys.llnl.gov/Organization /VDivision/Research/USP/USPFacilityVirtualTour/cpa.html. 1/30/03.

[2] J Collier et al. CPA Design Considerations for the Vulcan Petawatt Upgrade. Central Laser Facility Annual Report 1999/2000, 176.

[3] M. Perry. http://www.llnl.gov/str/Petawatt.html. 4/26/05

[4] Central Laser Facility. http://www.clf.rl.ac.uk/news/CLF_News/petawatt.htm. 11/30/04

[5] I. Geltner. A New Approach to Ultrashort Laser Pulse Amplification. Dissertation, Princeton University. (2003)

[6] V. M. Malkin, G. Shvets, N. J. Fisch. Ultra-powerful compact amplifiers for short laser pulses. Physics of Plasmas **7**, 5 2232 (2000)

[7] N. J. Fisch, V. M. Malkin, G. Shvets. Compression of High Power Lasers in Plasma. AIP Conference. Volume 611. 409-420. (2002)

[8] W. Cheng, Y, Avitzour, Y. Ping, S. Suckewer. Reaching the Nonlinear Regime of Raman Amplification of Ultrashort Laser Pulses. Phy. Rev. Let. **94,** 045003 (2005)

[9] G. Shvets, N. J. Fisch, A. Pukhov, and J. Meyer-ter-Vehn, Phys. Rev. Lett. **81**, 4879 (1998)

[10] Y. Ping, I. Geltner, and S. Suckewer, Phys. Rev. E **67**, 016401 (2003)

[11] Y. Ping, W. Chen, S. Suckewer, D. Clark, N. J. Fisch, Phy. Rev. Lett. **92**, 175007 (2004).

[12] N. Fisch. http://www.ofes.fusion.doe.gov/more_html/HEDPWORKSHOPRECORD /FIsch524.pdf. 12/20/04

[13] Y. Ping, I. Geltner, A. Morozov, N. J. Fisch, S. Suckewer, Phys. Rev. E **66**, 046401 (2002).

[14] Y. Ping, I. Geltner, S. Suckewer, Phys. Rev. E **67**, 016401 (2003)

[15] S. Augst, et al., Phy. Rev. Lett. **63**, 2212 (1989).

[16] E. W. Gaul et al., Phy. Rev. Lett. **77**, 4112 (2000).

[17] M.P. van Exter, J. Loaiza. Second-harmonic generation. http://www.physics.leidenuniv.nl/edu/courses/practicum_2/second-harmonic/second-harmonics5.pdf. 1/18/04

[18] M. Kalal. Fourier Based Analysis of Classical, Modulated and Complex Interferograms. 4/27/05

[19] M Takeda, H Ina, S Kobayashi, J . Opt. Soc. Am. **12** 156-60

[20] C Gorecki, Pure Appl. Opt. **1** 103-110 (1992)**.**

[21] M. Kalal and K Nugent. Abel Inversion Using Fast Fourier Transforms. Journal of Applied Optics **27** 10 (1988).

[22] G. Pretzler, Z. Naturforsch "A new method for numerical Abel-inversion," Teil A **46,** 639–641 (1991)

[23] Y. Ping, I Geltner, A Morozov, S. Suckewer. Interferometric Measurements of Plasma Density in Microcapillaries and Laser Sparks. Physics of Plasmas **7**, 11 (2002).

[24] P. Mannion, J. Magee, E. Coyne, G. O'Connor. Ablation Thresholds in Ultrafast Laser Micro-Machining of Common Metals in Air. Proceedings of SPIE Vol. 4876 (2003)

[25] C. Shafer, H. Urbassek, and L. Zhigilei. Metal Ablation by Picosecond Laser Pulses: A Hybrid Simulation. Phys. Rev. B **66** 115404 (2002).

[26] T. R. Clark and H. M. Milchberg, Phys. Plasmas **7**, 2192 (2000).

[27] T. R. Clark, and H. M. Milchberg, Phys. Rev. Lett. **78**, 2373 (1997).

[28] C. G. Durfee, J. Lynch, H. M. Milchberg. Development of a plasma waveguide for high-intensity laser pulses. Phys. Rev. E **51**, 3 (1995).

[29] P. Chessa, M. Galimberti, A. Giulietti, D. Giulietti, L. A. Gizzi, and P. Mora. Laser Energy Depoisition in Relativistic Interactions with Underdense Plasmas. Eur. Phys. Journal D **8**, 153-156 (2000)

[30] L. V. Keldysh, Zh. Eksp. Teor. Fiz. 47, 1945 (1964) Sov. Phys. JETP 20, 1307 (1965).

[31] C. G. Durfee and H. M. Milchberg. Light Pipe for High Intensity Laser Pulses. Phys. Rev. Letters, **71** 15 (1993)

[32] J. Fan, E, Parra, I. Alexeev, K. Y. Kim, and H. M. Milchberg. Tubular Plasma Generation with a High-power Hollow Bessel Beam. Physical Review E **62**, 6 (2000)

[33] Structure of Glow Discharge. http://science-education.pppl.gov/SummerInst

/SGershman/Structure_of_Glow_Discharge.pdf. 4/25/05

[34] H. Miller. Paschen Curve in Nitrogen. Journal of Applied Physics **34** 11 (3418)

[35] T. R. Clark and H. M. Milchberg, Phys. Rev. Lett. **81**, 357 (1998).

[36] D. J. Spence, A Butler, S. M. Hooker. First Demonstration of Guiding of High-intensity Laser Pulses in a Hydrogen-filled Capillary Discharge Waveguide. Journal of Physics B **34** 4103-4112 (2001)

[37] A. Zigler, Y. Ehrlich, and C. Cohen. Optical Guiding of High-intensity Laser Pulses in a Long Plasma Channel Formed by a Slow Capillary Discharge. Journal of the Opt. Soc. of America **13**, 1 (1996).

[38] J. Faure, V. Malka, J. R. Margues, F. Amiranoff. Interaction of an Ultra-intense Laser Pulse with a Nonuniform Preformed Plasma. Physics of Plasmas **7**, 7 (2000).

Appendix A

```
[FileName, PathName] = uigetfile('*.bmp','Select the BMP image');
if isequal(FileName,0)|isequal(PathName, 0)
    disp('File not found');
else
    full_file_name=strcat(PathName, FileName);
    a=imread(full_file_name);
    b=double(a);
    if  (sum(b',1)~=0)
        % even rows are black?
        EvenFlag = 1;
        k=3:2:479;
        c1=a;
        c1(1,:)=c1(2,:);
        c1(k,:)=0.5*(b(k-1,:)+b(k+1,:));
        % odd rows
        k=2:2:478;
        c2=a;
        c2(k,:)=0.5*(b(k-1,:)+b(k+1,:));
    else
        % odd rows are black?
        k=2:2:478;
        c1=a;
        c1(k,:)=0.5*(b(k-1,:)+b(k+1,:));
        % even rows
        k=3:2:479;
        c2=a;
        c2(1,:)=c2(2,:);
        c2(k,:)=0.5*(b(k-1,:)+b(k+1,:));
    end
    imshow(c1);
    new_file_name = strrep(full_file_name,'.bmp','.jpg');
    button = questdlg('Is this image restored correctly?','Select correctly restored
image','Yes','No','Yes');
    if strcmp(button,'Yes')
        imwrite(c1, new_file_name);
    elseif strcmp(button,'No')
        imshow(c2);
        button = questdlg('Is this image restored correctly?','Select correctly restored
image','Yes','No','Yes');
            if strcmp(button,'Yes')
                imwrite(c2, new_file_name);
            elseif strcmp(button,'No')
                errordlg('Image cannot be restored','Processing Error');;
            end
    end
end
```

Appendix B

```
clear global;
[FileName, PathName] = uigetfile('*.bmp','Select the line image');
if isequal(FileName,0)|isequal(PathName, 0)
    disp('File not found');
else
    full_file_name=strcat(PathName, FileName);
    img=imread(full_file_name);
    figure(1), imshow(img);
    img_dbl=double(img)';
    [vert,N_img]=size(img_dbl);
    [dummy,minima]=min(img_dbl);
    minima_sm=smooth(minima,19,'sgolay',2);
% 18.5 is the period of non-disturbed lines (in pixels).
% This period is calculated by a code "Frequency".
    phase_shift=(minima_sm-min(minima_sm))/18.6;
    clear dummy minima minima_sm img img_dbl;
% Abel transform: constructor for h_y
%
% 59 is the coordinate of the middle point of the channel.
% This coordinate is taken from the data visualized by Excell.
    N0=59;
    dy0=180/(248-205); %um
    k0=1:N0;
    R=N0*dy0;
    y0=k0.*dy0;
    h_y0=flipud(phase_shift(k0));
% Abel inersion: interpolation of h_y
    N=300;
    k=0:N;
    dy=R/N;
    y=k.*dy;
    h_y=interp1(y0,h_y0,y,'spline');
    figure(2),plot(y0,h_y0,y,h_y);

% Abel inversion: frequency range setting
    Nlow=0;
    Nhigh=400;
    n=(Nlow:Nhigh)';
% Abel inversion: pre-tabulated f_ni
    g=cos(pi*(n*y)/R);
    f=((-1).^n)*ones(size(y));
    f_ni=1-g.*f;
    f_ni(n+1,N+1)=1-(-1).^n.*cos(n.*pi/1.01);
    f_ni(1,:)=1;
    clear f g;
% Abel inversion: pre-tabulated c_ik without diagonal elements
    a=(y.^2)'*ones(size(y));
```

```
   b=ones(size(y))'*(y.^2);
   c=(sqrt(a-b));
   c=tril(c);
   e=1.0e-8*ones(size(y))'*ones(size(y));
   c=c+triu(e);
   d=dy*y'*ones(size(y));
   d=d./c;
   c_ik0=(d-triu(d));
   clear a b c d e;
% Abel inversion: addition of diagonal elements to c_ik
   m=ones(size(y))'*sqrt(2*dy*y+dy^2);
   e=triu(m)-(m-tril(m));
   c_ik=c_ik0+e*1.5;
   clear m e c_ik0;
% Abel inversion: calculation of h_nk
   h_nk=f_ni*c_ik;
% Abel inversion: calculation of B_nm
   B_nm=2*h_nk*h_nk';
% Abel inversion: calculation of C_m
   C_m=h_y*h_nk';
% Abel inversion: solution of linear equation A_n*B_nm=C_m
   A_n=C_m/B_nm;
% Abel inversion: calculaton of inverted function f_y
   f_r=A_n*f_ni;
% Saving the results
   lambda=0.532;          % um
   n_cr=1.1e21/(lambda^2); % cm-3
   n_r=f_r*n_cr*lambda;
   figure(3), plot(y,n_r);
   new_file_name = strrep(full_file_name,'.bmp','_density.csv');
   ans = [y; n_r];
   fid = fopen(new_file_name,'w');
   fprintf(fid,'%e, %e\n', ans);
   fclose(fid);
end
```